scientific reports

OPEN

Enhanced photocatalytic degradation of Acid Blue dye using CdS/TiO₂ nanocomposite

Nida Qutub[1]✉, Preeti Singh[1,2]✉, Suhail Sabir[3], Suresh Sagadevan[4]✉ & Won-Chun Oh[5]✉

Photocatalytic degradation is essential for the successful removal of organic contaminants from wastewater, which is important for ecological and environmental safety. The advanced oxidation process of photocatalysis has become a hot topic in recent years for the remediation of water. Cadmium sulphide (CdS) nanostructures doped with Titanium oxide (CdS/TiO₂) nanocomposites has manufactured under ambient conditions using a simple and modified Chemical Precipitation technique. The nanocomposites crystal structure, thermal stability, recombination of photo-generated charge carriers, bandgap, surface morphology, particle size, molar ratio, and charge transfer properties are determined. The production of nanocomposites (CdS-TiO₂) and their efficient photocatalytic capabilities are observed. The goal of the experiment is to improve the photocatalytic efficiency of TiO₂ in the visible region by doping CdS nanocomposites. The results showed that as-prepared CdS-TiO₂ nanocomposites has exhibited the highest photocatalytic activity in the process of photocatalytic degradation of AB-29 dye, and its degradation efficiency is 84%. After 1 h 30 min of visible light irradiation, while CdS and TiO₂ showed only 68% and 09%, respectively. The observed decolorization rate of AB-29 is also higher in the case of CdS-TiO₂ photocatalyst ~ 5.8×10^{-4} mol L⁻¹ min⁻¹) as compared to the reported decolorization rate of CdS ~ 4.5×10^{-4} mol L⁻¹ min⁻¹ and TiO₂ ~ 0.67×10^{-4} mol L⁻¹ min⁻¹. This increased photocatalytic effectiveness of CdS-TiO₂ has been accomplished by reduced charge carrier recombination as a result of improved charge separation and extension of TiO₂ in response to visible light.

Wastewater recycling by photocatalysts could be a solution to many countries' long-standing freshwater shortages[1]. Water pollution-related environmental issues have been a serious issue in recent decades, negatively affecting human health and the ecology. Access to safe drinking water has risen to the top of the priority list for long-term economic growth and societal well-being. Water is necessary for life and a valuable resource for civilization; it also plays an important role in natural ecosystems and climate regulation. Water stress is largely a problem of scarcity of water, but it can also be caused by deterioration of water quality and a lack of proper water management[2]. Wastewater from the pulp, leather, fabric, polymer, pesticide and pharmaceutical sectors comprises a variety of organic contaminants, including dyes, that contaminate water and harmful life on the planet[3–5]. Separating and degrading these organic waste products has taken precedence in ensuring a nontoxic and pollution-free environment[6]. Photocatalysis an advanced oxidation process (AOP) is currently being utilized to remove colours from water without producing any hazardous by-products[6]. Fujishima and Honda[7] established the theory of photocatalysis, which focuses on the generation of highly reactive intermediates, such as hydroxyl radicals ($\cdot$OH), which rapidly oxidize a wide range of pollutants. The photocatalyst's catalyst activity is highly dependent on the light sources; ultraviolet (UV) radiations have also been used[8–10]. A photocatalyst is a compound that facilitates the acceleration and enhancement of a light-induced reaction without being consumed. A photocatalyst turns solar energy into chemical energy, which can be utilized for pollution and sustainable applications such as water purification, environmental remediation, self-cleaning surfaces, hydrogen synthesis via water cleavage, and CO₂ conversion to hydrocarbon fuels. Solar energy is the purest and most abundant source of radiating energy that does not include any contaminants[11].

[1]Department of Chemistry, Jamia Millia Islamia, New Delhi 110025, India. [2]Department of Fibers and Textile Processing Technology, Institute of Chemical Technology, Mumbai 400019, India. [3]Department of Chemistry, Aligarh Muslim University, Aligarh 202002, India. [4]Nanotechnology & Catalysis Research Centre, University of Malaya, 50603 Kuala Lumpur, Malaysia. [5]Department of Advanced Materials Science and Engineering, Hanseo University, Seosan-si 356-706, Chungnam, Korea. ✉email: drnidaqutub@gmail.com; aries.pre84@gmail.com; drsureshnano@gmail.com; wc_oh@hanseo.ac.kr

In recent times, lot of interest in the development of novel photocatalytic technologies for a wide range of environmental applications, such as water remediation, oil spill and another pollution cleaning. Some energy-related research has focused on the utilization of photocatalysts for fuel production (e.g., H_2), specifically through water splitting[12]. Solar radiation is used to convert pollutants from complicated molecules to simple and nontoxic compounds, avoiding the need for additional treatment, disposal, or the use of expensive oxidizing chemicals. Titanium oxide nanoparticle (TiO_2 NP) is widely used as a photocatalyst in the field of advanced oxidation technology due to its advantageous properties, such as exceptional optical and electronic properties, strong oxidative power, high photocatalytic efficiency, high stability, robust physical and chemical stability, low cost, low toxicity, stability in aqueous solutions, and eco-friendliness[13,14]. It is a well-known potent photocatalyst for degrading a wide range of molecules[15], including inorganic and organic compounds[16,17]. Titanium oxide (TiO_2) photocatalytic activity is influenced not only by its bulk energy band structure, but also by the crystalline structure, textural characteristics, surface area, and particle size of the TiO_2 powder[18]. The photocatalytic activity of TiO_2 can be improved by changing the physicochemical nature of the nanoparticle surface to increase the adsorption of harmful compounds to be destroyed and reduce the likelihood of charge carrier recombination[19,20].

In the previous two decades, there has been substantial progress in the creation of effective photocatalytic materials, with a high number of research articles released each year. Advances in nanotechnology have substantially connected with improvements in the performance of photocatalytic materials. Titanium dioxide has been extensively explored for photocatalysis because it has numerous advantages such as strong photocatalytic activity, great physical and chemical stability, low cost, non-corrosive, non-toxicity, and high availability[21,22]. When TiO_2 NP absorbs light at 385 nm, electrons (e^-) are excited from the valence band to the conduction band, leaving a positively charged vacancy known as a hole (h^+)[23]. The hole is a strong potent oxidizing agent in and of itself, and in the presence of water and molecular oxygen, it can generate hydroxyl radicals or directly oxidize adsorbed molecules on the NP surface. TiO_2 has the advantage of being able to execute functions while using sunlight as a source of energy. Due to charge recombination, these photoinduced charges have a relatively brief lifetime, releasing the absorbed light energy as heat with no chemical consequence. These charges can also migrate to lower-energy trap sites, where they can still recombine or participate in redox processes with adsorbed species. As a result, preventing electron–hole recombination is critical for improving TiO_2 efficiency. Furthermore, TiO_2 can only absorb in the UV area of the solar spectrum, which accounts for just about 5% of total solar energy falling on the earth's surface[24], restricting its application. As a result, numerous attempts have been made to increase charge separation by altering the surface or bulk properties of TiO_2, such as doping[25], metal deposition[26], size reduction, and coupling of two semiconductors, consequently boosting photocatalytic activity[27,28]. The photo-response of TiO_2 can be improved by combining it with a semiconductor that has a smaller bandgap and a higher conduction band than TiO_2. To begin with, a narrow bandgap will boost solar energy absorption efficiency by pushing it into the visible range. Second, photogenerated electrons in the narrow bandgap SC's conduction band (CB) will be injected into TiO_2's CB, reducing charge recombination and keeping oxidation and reduction processes in different reaction sites[29]. TiO_2 has a bandgap of 3.2 eV for the anatase phase and 3.0 eV for the rutile phase, respectively. As a result, under visible light irradiation, TiO_2 is nearly inert, making it unable to use solar energy sustainably[30].

On the other hand, TiO_2 has a number of disadvantages that limit its use in photocatalysis. To begin with, photogenerated electrons and holes coexist in the titania particle, with a high likelihood of recombination. As a result, the desired chemical changes occur at modest rates in relation to the absorbed light energy. Because of the very large bandgap energy (3.2 eV), photoactivation requires ultraviolet light, resulting in very low efficiency in utilizing solar radiation. When compared to visible light, UV light makes up just around 5% of the solar spectrum (45% only)[31–33]. Furthermore, due to its non-porous nature and polar surface, titania has a poor absorption capacity for non-polar organic contaminants[34]. The recovery of nano-sized titania particles from treated water is also a challenge, both economically and in terms of safety[35]. Agglomeration and aggregation alter the photo-activity and light absorption of TiO_2 nanoparticles[36–38]. To alleviate these limitations, several techniques have been proposed in the open literature. These strategies aim to increase the utilization of solar energy by extending the wavelength of photoactivation of TiO_2 into the visible region of the spectrum; preventing electron/hole pair recombination and thus allowing more charge carriers to diffuse to the surface; increasing the adsorption affinity of TiO_2 towards organic pollutants, and preventing aggregation and agglomeration of nano-titania particles while easing their recovery. Many efforts have been made to improve TiO_2 NPs immobilised on TiO_2 nanofibers (TNF), making them a promising platform for photocatalytic wastewater treatment and other applications such as sensing, photovoltaics, and photocatalytic water splitting[39–41]. Furthermore, recent advances in the design and engineering of metal oxide–graphene–noble metal-based high-performance photocatalyst systems are developed, with an emphasis on the associated mechanisms and their applications in various photocatalytic processes[42,43]. Several reviews on the development of ways to overcome the limits of titania photocatalysis have been published in recent years[44–47]. Ion doping, for example, anatase–rutile phase coexisting[48], ion doping[49], or p-n heterojunction formation[50]. Many elements were doped into TiO_2, such as Ag^{51}, Fe^{52}, $N^{53,54}$, S^{55}, C^{56} and B^{57}, etc. Doping ions can introduce new energy levels into TiO_2, lowering the bandgap energy and increasing photocatalytic activity, especially when exposed to visible light. Consequently, the development of charge trapping sites by foreign ions can effectively lower the rate of electron–hole recombination[58].

On the other hand, Cadmium sulphide (CdS) is an excellent photocatalyst in the visible region but has low quantum efficiency due to low stability in solution due to Cd^{2+} ion leaching. As a result, despite its relatively high photoactivity, significant efforts are being made to increase photocatalytic stability. Attempts to improve the photocatalytic efficiency of CdS have included changing the surface structure of CdS NPs by controlling morphology, doping transition metal ions into CdS, depositing CdS to Nafion membranes, graphene sheets, or carbon nanotubes to obtain a uniform, homogeneously distributed CdS QDs, and coupling CdS with another semiconductor. Combining different bandgap semiconductors to make solid solutions is an effective approach

to adjust the potential of conduction and valence bands by making successive composition changes[59]. Due to the suitable band gap (2.4 eV) of CdS[60], lower CB than TiO$_2$, great optical property, and possible application of CdS in photo-electrochemistry, photocatalysis, and water splitting systems, coupling of TiO$_2$ with cadmium sulphite (CdS) has been widely researched[61]. Due to its low bandgap (2.4 eV), which enables its visible light response, CdS is the most important chalcogenides semiconductor as a hydrogen production catalyst[62,63]. The restricted separation efficiency of photogenerated charge carriers can overcome either by employing CdS in the form of QDs due to a shorter transit path or by integrating CdS onto support materials, such as TiO$_2$[64,65].

CdS doped TiO$_2$ nanotube composites were previously synthesized by chemical bath deposition, and their light-harvesting performance was 2.9 times than that of pure TiO$_2$ nanotubes. Under UV light irradiation, the CdS doped TiO$_2$ nanotube composite had better photocatalytic activity and photodegradation efficiency than pure TiO$_2$ nanotube and the degradation efficiency of methyl orange was about 42 percent at a UV intensity of 32 W[66]. Rao et al.[67] created CdS/TiO$_2$ core/shell nanorods with variable shell thickness to reduce charge carrier recombination and photo corrosion when exposed to UV–Vis light. Du et al. created the same type of composite, but with different morphology, by fabricating pyramid-like CdS nanoparticles and growing them on porous TiO$_2$. The H$_2$ generation rate of 5 mol% CdS-TiO$_2$ was 1048.7 mol h^{-1} g^{-1} under UV–Vis irradiation and without noble-metal co-catalysts, which is about six times and 1.5 times greater than pure TiO$_2$ and CdS, respectively[68].

In the present study, a series of TiO$_2$ NPs were synthesized in this study to investigate the effect of reactant concentration on size, shape, crystal structure, thermal, optical, and photocatalytic activities. According to prior research, a number of manufactured CdS NPs were used in the photocatalytic experiment, and it was discovered that the CdS NPs, has an excellent photo-response, but not suitable for photocatalytic water purification. TiO$_2$ is not photoactive under the visible region of the solar spectrum. Thus, in order to make CdS potentially applicable for water purification and utilization of TiO$_2$ in the visible region a nanocomposite of cadmium sulphide and titanium dioxide (CdS-TiO$_2$) was also synthesized and the effect of CdS on TiO$_2$ and vice versa was studied.

Materials and methods

Synthesis of titanium oxide nanoparticle (TiO$_2$ NP) by precipitation technique. Controlled precipitation of nanoparticles from precursors dissolved in a solution was used to make TiO$_2$ NP. The reductive hydrolysis of Titanium Tetra Isopropoxide (TTIP) in methanol at ambient temperature and pressure without calcinations was proposed for the manufacture of TiO$_2$ nanoparticles[69]. By adjusting the concentration of TTIP while maintaining the amount of methanol (24.44 M) constant at 100 mL, a series of TiO$_2$ NP (Tma, Tmb, Tmc, Tmd, and Tme) was synthesized. Tma = 0.25 M, Tmb = 0.20 M, Tmc = 0.15 M, Tmd = 0.1 M, and Tme = 0.05 M have different TTIP concentrations. The reactions were carried out as follows: 100 mL methanol (24.44 M) was placed in a conical flask, and TTIP was added dropwise (20 drops per minute) while vigorous stirring continued for another 5 h. White precipitates observed were washed with water and acetone several times and then air-dried. The crystal structure of the produced TiO$_2$ was expected to be a mix of anatase, brookite, and rutile.

Chemical route for the synthesis of cadmium sulphite doped titanium oxide (CdS-TiO$_2$). In a reaction vessel, 100 mL aqueous Cd (NO$_3$)$_2$ (0.085 M) was added dropwise with continuous stirring, followed by 50 mL methanol (24.44 M). The reaction was then carried out for 1 min in the H$_2$S environment with vigorous stirring and then continued for another 2 h. The colour of the solution changed from clear to yellow. 3.53 mL TTIP (0.1 M) was added drop-by-drop to this solution (20 drops per minute). The stirring was extended for another 5 h. The hue of the solution had changed to a faint yellow.

Characterization techniques. The synthesized TiO$_2$ NP and CdS-TiO$_2$ NC were characterized by elemental, structural, optical and thermal techniques. Elemental analysis and chemical compositions were examined by energy-dispersive X-ray spectroscopy (EDS, JEOL, JSM6510LV) and Fourier Transform Infrared Spectroscopy. The structural properties were analysed by employing powder X-ray diffraction (Miniflex-TM II Benchtop, Rigaku Co-operation, Tokyo, Japan). Surface morphology and size was characterized by Scanning Electron Microscopy (JEOL, JSM6510LV) and Transmission Electron Microscopy (JEOL, JEM2100). Thermal properties were determined by Thermal Gravimetric Analysis (TGA). The optical properties were determined by employing UV–Visible Spectroscopy (Shimadzu UV-1601).

Photocatalytic experiment. The decolorization of a dye derivative Acid Blue-29 (AB-29) in the presence of UV light was used to investigate the photocatalytic activity of TiO$_2$ nanoparticles. The photocatalytic studies were carried out in an immersion well Pyrex glass photoreactor (inner and outer jacket) with a magnetic bar, water circulating jacket, and a molecular oxygen opening. A 125 W medium pressure mercury lamp was used to irradiate the area (Philips). The optimal catalyst dosage was established by irradiating the dye (AB-29) aqueous solution with various strengths of TiO$_2$ nanoparticles. 180 mL dye (AB-29) solution (0.06 mM) containing manufactured nanocatalysts (1 g L^{-1}) were magnetically swirled in the dark for at least 20 min in the presence of ambient oxygen to achieve dye (AB-29) and nanocatalyst surface adsorption–desorption equilibrium. After reaching equilibrium, the first aliquot (5 mL, 0 min) was removed and the irradiation process began. During the irradiation, other aliquots of 5 mL were taken at regular intervals and examined following centrifugation. Changes in absorption were used to track the decolorization of AB-29 using a UV–Visible spectroscopic analysis approach (Shimadzu UV–Vis 1601). The dye concentration was determined using a standard calibration curve based on the dye's absorbance at various known values. The photocatalytic activity of the CdS-TiO$_2$ nanocomposite was tested by examining the decolorization of AB-29 in the presence of visible light using a halogen linear lamp (500 W, 9500Lumens) as a light source and comparable experimental conditions as described before. Photocatalytic studies were conducted for five cycles using the same batch of nanomaterial photocatalysts to
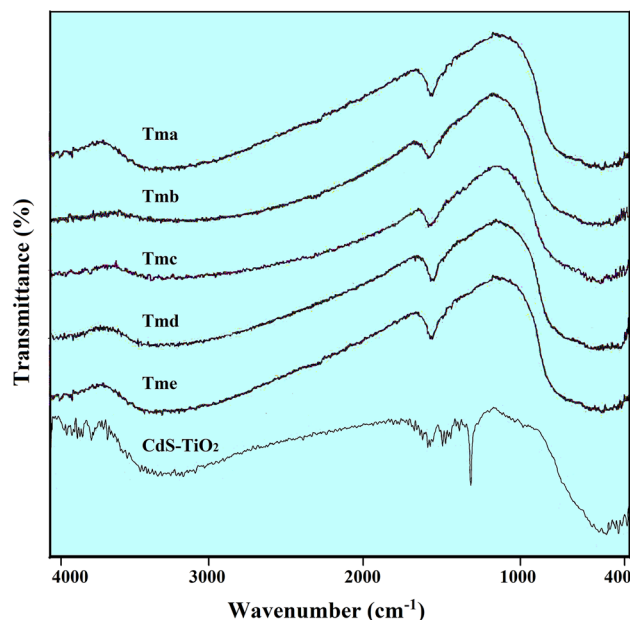
Figure 1. The FTIR Spectra of the synthesized TiO_2 nanoparticles (Tma, Tmb, Tmc, Tmd and Tme) and its nanocomposites with CdS (CdS-TiO_2).

Peak	Range	Intensity	Significance
A	(400–420)	Small and weak	Cd-S bond (CdS nanoparticles)
B	(400–800)	broadband	Ti–O bond vibration (TiO_2 nanoparticles)
C	(570–620)	Small and weak	S–S bond (crystal S–S bond)
D	(1380–1420)	Sharp or Broad	C–H bending of CH_3 (Acetone)
E	(1620–1740)	Small and weak	CO_2 bending or C–H bending (Acetone)
F	(3140–3470)	Broad	Intermolecular H-bonds (Lattice water)

Table 1. Significance of peaks obtained in the FTIR spectra of the synthesized TiO_2 nanoparticles (Tma, Tmb, Tmc, Tmd and Tme) and CdS-TiO_2.

determine the reusability and recyclability of the nanomaterials as catalysts. Before each photocatalytic run, the nanocomposite catalyst was rinsed with double distilled water after each cycle and a fresh solution of AB-29 was added.

Results and discussion

Spectroscopy analysis. The purity and composition of the samples were validated by FTIR spectra as shown in Fig. 1, which revealed multiple peaks related to TiO_2 in all samples without any other elemental contamination. In the 800–400 cm^{-1} area, bands for Ti–O and Ti–O–Ti bands were detected. The FTIR spectra of TiO_2 could be in the form of a broad band centred at 400–800 cm^{-1} due to the Ti–O bond vibration in the TiO_2 lattice[70] or peaks centred at 760 cm^{-1}, 680 cm^{-1}, 600 cm^{-1}, 560 cm^{-1}, 500 cm^{-1}, 468 cm^{-1}, 410 cm^{-1}, 385 cm^{-1} and 350 cm^{-1} attributable to[71,72]. The FTIR spectra of TiO_2 nanoparticles (Tma, Tmb, Tmc, Tmd, and Tme) and their nanocomposites with CdS are shown (CdS-TiO_2) in Fig. 1. The varied peaks generated by TiO_2 nanoparticles and their nanocomposites with CdS nanoparticles are explained in Table 1[73,74].

The FTIR spectra of TiO_2 NPs (Tma, Tmb, Tmc, Tmd, and Tme) and CdS-TiO_2 NC in this study were in the shape of a large peak in the 400–800 cm^{-1} region with multiple tiny peaks. Stretching Vibrations of hydroxyl (OH) groups of water adsorbed by the samples were ascribed to the broad peak showing at 3100–3600 cm^{-1}. Such TiO_2–OH groups are formed as a result of the hydrolysis reaction in the process. The bending modes of –OH groups of water molecules adsorbed on the surface of the catalyst are responsible for the peak at 1628 cm^{-1}[75]. CO_2 deposited on the surface of the particles showed a weak absorption band at 1620–1630 cm^{-1}. Adsorption of water and CO_2 was ubiquitous for all powder samples exposed to the atmosphere, and significantly more evident for nanosized particles with large surface areas, as well known[75]. In the case of CdS-TiO_2, the existence of a broad band centred at 400–800 cm^{-1} with numerous little peaks in it proved the creation of CdS, and the presence of broadband centred at 400–800 cm^{-1} with several small peaks in it indicated the presence of TiO_2 in the nanocomposite. The creation of a sandwich structure with CdS at the centre (core) and TiO_2 NPs surrounding CdS as a shell result in CdS stretching at 605 cm^{-1}. The FTIR spectra of the reaction product, obtained
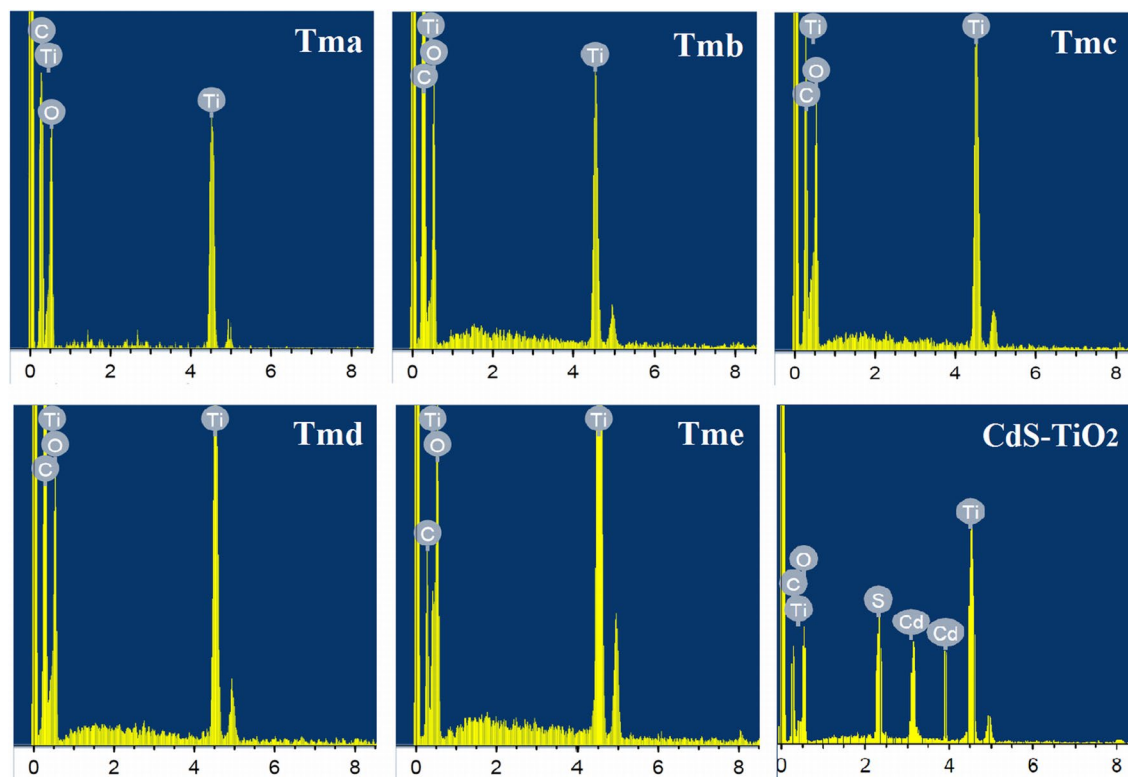
Figure 2. EDAX of the synthesized TiO_2 nanoparticles (Tma, Tmb, Tmc, Tmd and Tme) and its nanocomposites with CdS (CdS-TiO_2).

after heating the precursor at 300 °C for 2 h, reveal no absorption peak in the upper-frequency area but a sharp peak below 500 cm^{-1}, which could be attributable to the Ti–O–Ti bond stretching frequency modes in titanium dioxide[76]. Individual bands at 675 cm^{-1} may be related to the anatase phase, and are attributed to Ti–O bond stretching vibration[77]. Stretching vibrations of functional groups CH, CH$_2$, and CH$_3$ are represented by the bands at 2963, 2907, and 2809 cm^{-1}. At 1600 cm^{-1}, the vibration corresponds to the C=C bond stretching vibration. The bands in the 1500–1400 cm^{-1} range are caused by bending vibrations of CH, CH$_2$, and CH$_3$, while those in the 1300–1200 cm^{-1} range are caused by vibrations of the methoxy group O-CH$_3$ and the alcohol group C–OH[78].

Energy dispersive X-ray spectroscopy (EDAX) analysis. Figure 2 shows the EDAX spectra of the prepared samples. For the samples Tma, Tmb, Tmc, Tmd, and Tme, the spectra revealed the existence of Ti and O peaks, confirming the synthesis of pure TiO_2 with no other elemental impurity. The other peaks in this graph, related to oxygen, carbon, and silicate, were caused by the sputter coating of the glass substrate on the EDS stage and not taken into account. The presence of peaks corresponding to Cd and S, as well as peaks for Ti and O, in the EDS spectra of CdS-TiO_2 confirmed the creation of the CdS-TiO_2 nanocomposite.

Structural analyses. Diffraction and microscopic examinations were used to conduct structural evaluations. X-Ray Diffraction (XRD) Spectroscopy was used to conduct diffraction research. Due to the physical nature of the materials, the diffraction patterns for TiO_2 NPs (Tma, Tmb, Tmc, Tmd, and Tme) were of poor quality. The XRD pattern of the produced TiO_2 NPs (Tma, Tmb, Tmc, Tmd, and Tme) confirmed the existence of anatase, brookite, and rutile mixes (Fig. 3). TiO_2 NPs peaks are corresponded to anatase at 2θ = 25.56° (101), 37.8° (103), 48.07° (200), 54.18° (105), 62.42° (204) and 75.2° (215), rutile at 2θ = 27.01° (110), 36.14° (101), 42.121° (111), 54.89° (211) and 68.72° (301)[79,80] and brookite at 2θ = 30.9° (121)[49] thus confirming the presence of mixed crystal phase. Due to the presence of mixed peaks of anatase, rutile, and brookite TiO_2, estimating crystallite size for TiO_2 samples (Tma, Tmb, Tmc, Tmd, and Tme) based on the X-ray diffraction peak was not achievable. The XRD pattern of CdS-TiO_2 nanocomposites (Fig. 4) demonstrated the production of cubic CdS and anatase TiO_2 nanoparticles. The appearance of peaks at 2θ = 25.56 (101), 37.282 (103), 48.07 (200), 54.18 (105), and 62.42 (204), which corresponded only to anatase TiO_2, was linked to the synthesis of anatase TiO_2 in CdS-TiO_2[80,81]. The appearance of peaks that corresponded only to cubic CdS at 2θ = 26.719 (111), 29.900 (200), 43.000 (220), and 51.061 (311)[82,83] verified the production of cubic CdS. The existence of mixed peaks of cubic CdS and anatase TiO_2 made it impossible to estimate crystallite size for CdS-TiO_2 using the X-ray diffraction peak.

Scanning electron microscopy (SEM) analysis. SEM images of the synthesized TiO_2 NP are depicted in Fig. 5a–e. The creation of well-defined spherical mesoporous TiO_2 nanoclusters observed using SEM micro-
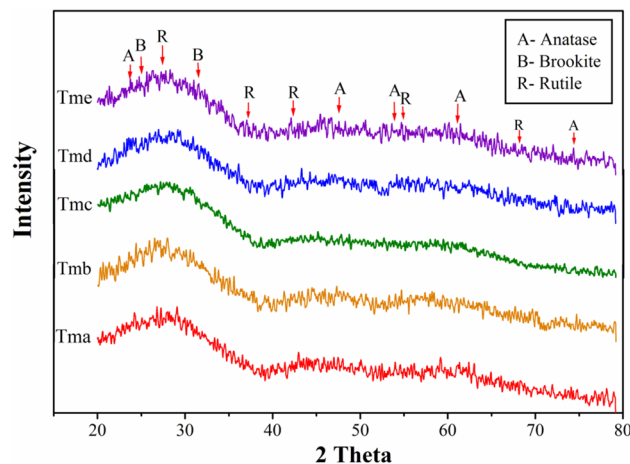
5

Figure 3. XRD patterns of synthesized TiO_2 nanoparticles (Tma, Tmb, Tmc, Tmd and Tme).
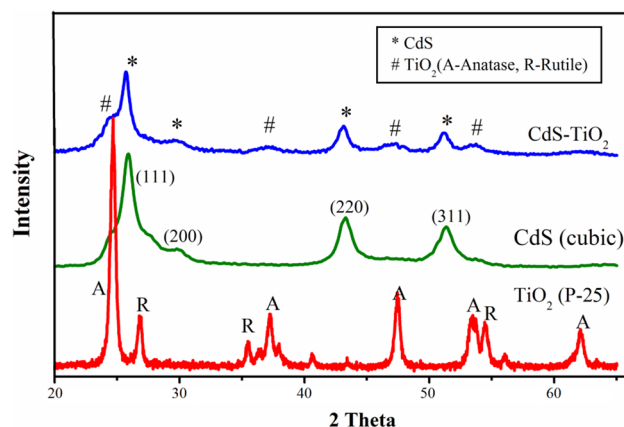

Figure 4. XRD pattern of CdS-TiO_2 nanocomposites in comparison to pure cubic CdS and Degussa P-25 TiO_2.

graphs was attributed to the high surface energy of nanosized TiO_2 particles[84]. By agglomerating tiny particles, pure TiO_2 generates a layer-like structure. An amorphous mass with a very small particle structure was visible in the SEM picture of CdS-TiO_2. Due to the thin amorphous powder, no other distinct particle shape was discernible as CdS particles uniformly covered by the TiO_2 nanoparticles formed a sandwich-type structure. in which CdS is acting as a core surrounded by smaller TiO_2 NPs. SEM pictures of the synthesized CdS-TiO_2 NC are shown in Fig. 5f[85].

Transmission electron microscopy (TEM) analysis. Figure 6a–f shows a TEM micrograph of TiO_2 NP (Tma, Tmb, Tmc, Tmd, and Tme). The creation of spherical nanoclusters made up of very small TiO_2 NPs (1–2 nm) can be seen in the images. The nanocluster size has shrunk from > 500 nm (Tma) to 50 nm (Tme). In all cases, however, the individual TiO_2 nanoparticles were smaller than 2 nm.

The TEM picture of CdS-TiO_2 (Fig. 7) verifies the presence of two different-sized nanoparticles CdS and TiO_2 nanoparticles with close proximity to each other. TEM images of CdS-TiO_2 (Fig. 7a) show two different-sized nanoparticles with smaller ones surrounding the larger ones in a core–shell type fashion. Further, the presence of both CdS and TiO_2 were also confirmed by EDS and XRD test results individually. The observed two distinctly different sized particles with close proximity to each other is the direct prove of the sandwich-type model of nanoparticles with smaller particles (TiO_2) surrounding the larger particle (CdS) like a core. Figure 7b shows a TEM image of the CdS-TiO_2 composite. Table 2 shows the particle sizes acquired using TEM.

Thermal analyses. The Thermal Gravimetric Analysis (TGA) graphs were used to conduct thermal experiments. TGA findings of the synthesised TiO_2 nanoparticles (Tma, Tmb, Tmc, Tmd, and Tme) and CdS-TiO_2 nanocomposite are shown in Fig. 8. The TGA curve demonstrated great thermal stability, the lack of any impurity or intermediate complex, and a high melting point for the produced nanoparticles. The TiO_2 NPs (Tma,
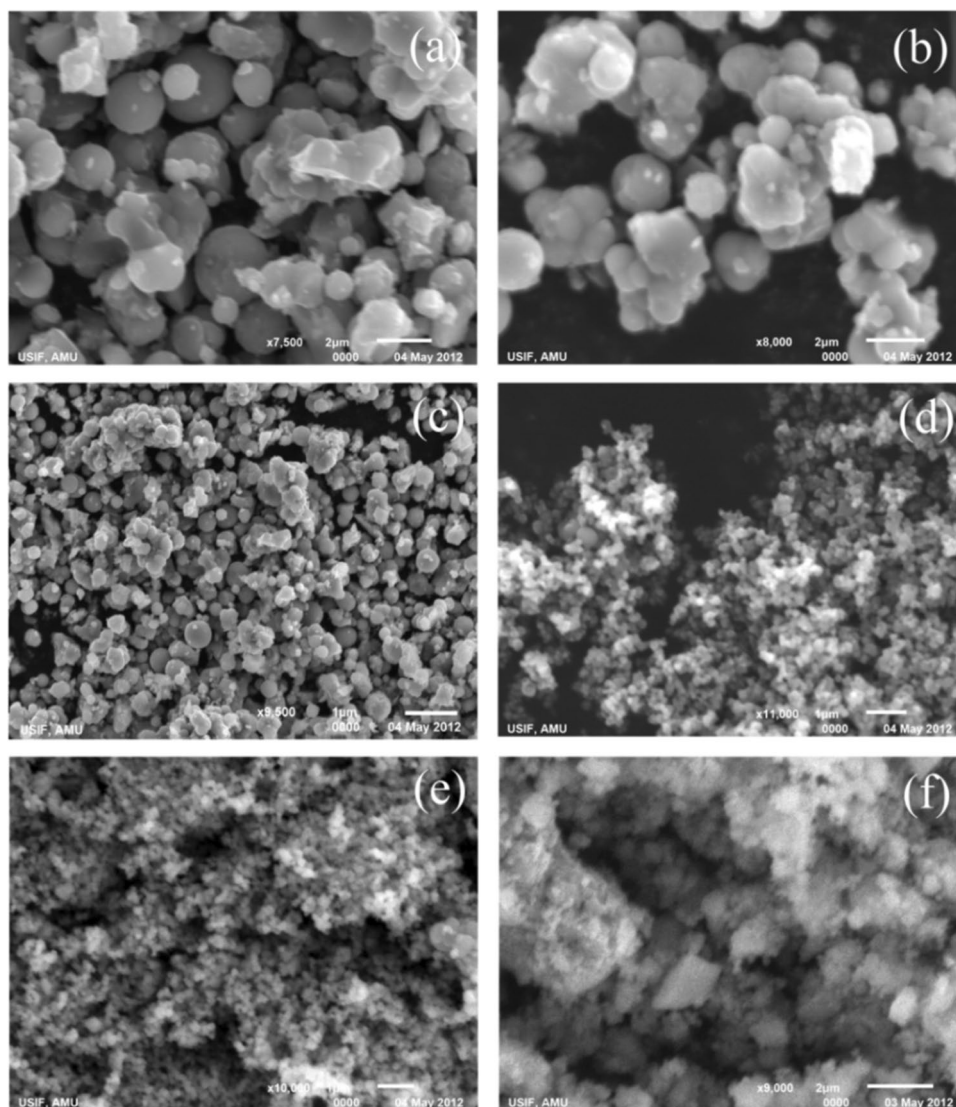
Figure 5. SEM images (**a**) Tma, (**b**) Tmb, (**c**) Tmc, (**d**) Tmd, (**e**) Tme and (**f**) CdS-TiO$_2$.

Tmb, Tmc, Tmd, and Tme) and CdS-TiO$_2$ NC were shown to be thermally stable up to 1000 °C, with a slight weight loss roughly at 100 °C, owing to the presence of moisture and other volatile solvents.

Optical analysis. The optical properties were determined using the UV–Visible absorption spectra. Figure 9a shows the absorption spectra of TiO$_2$ nanoparticles synthesized in the range of 350 nm to 600 nm range of the light spectrum. The absorption edge in bulk TiO$_2$ for anatase is 387 nm (3.2 eV), rutile is 410 nm (3.02 eV), and brookite is 381 nm (3.25 eV)[86,87]. The absorption edges of produced TiO$_2$ nanoparticles (Tma, Tmb, Tmc, Tmd, and Tme) were found to be in the wavelength range 382–403 nm, implying the presence of mixed phases or a blue shift from the bulk rutile phase. This blue shift was detected with the decrease of TiO$_2$ NP particle sizes from Tma to Tme, and was in good agreement with previous findings. This change was linked to QSE or the presence of TiO$_2$ mixed-phase[88]. XRD results given in the study indicated the presence of mixed-phase TiO$_2$. The values of the absorption edges of the different TiO$_2$ NPs are listed in Table 3.

Figure 9b shows the bandgap energy of TiO$_2$ NP. The bandgap curve was plotted (αhν)$^{1/2}$ vs hν based on Tauc relation revealed an indirect bandgap[89]. As the size of TiO$_2$ NP reduced from Tma to Tme, a greater band gap was observed.

Table 3 lists the corresponding band gaps of the various TiO$_2$ NPs. The bandgap of TiO$_2$ can also be calculated using the Eq. (1):

$$E_g = 1240/\lambda_{onset} \tag{1}$$

where E$_g$ denotes the bandgap energy, and onset denotes the absorption edge as determined by the absorption spectra[90]. The results of the above formula were in good agreement with the Tauc relation curves (Table 3).
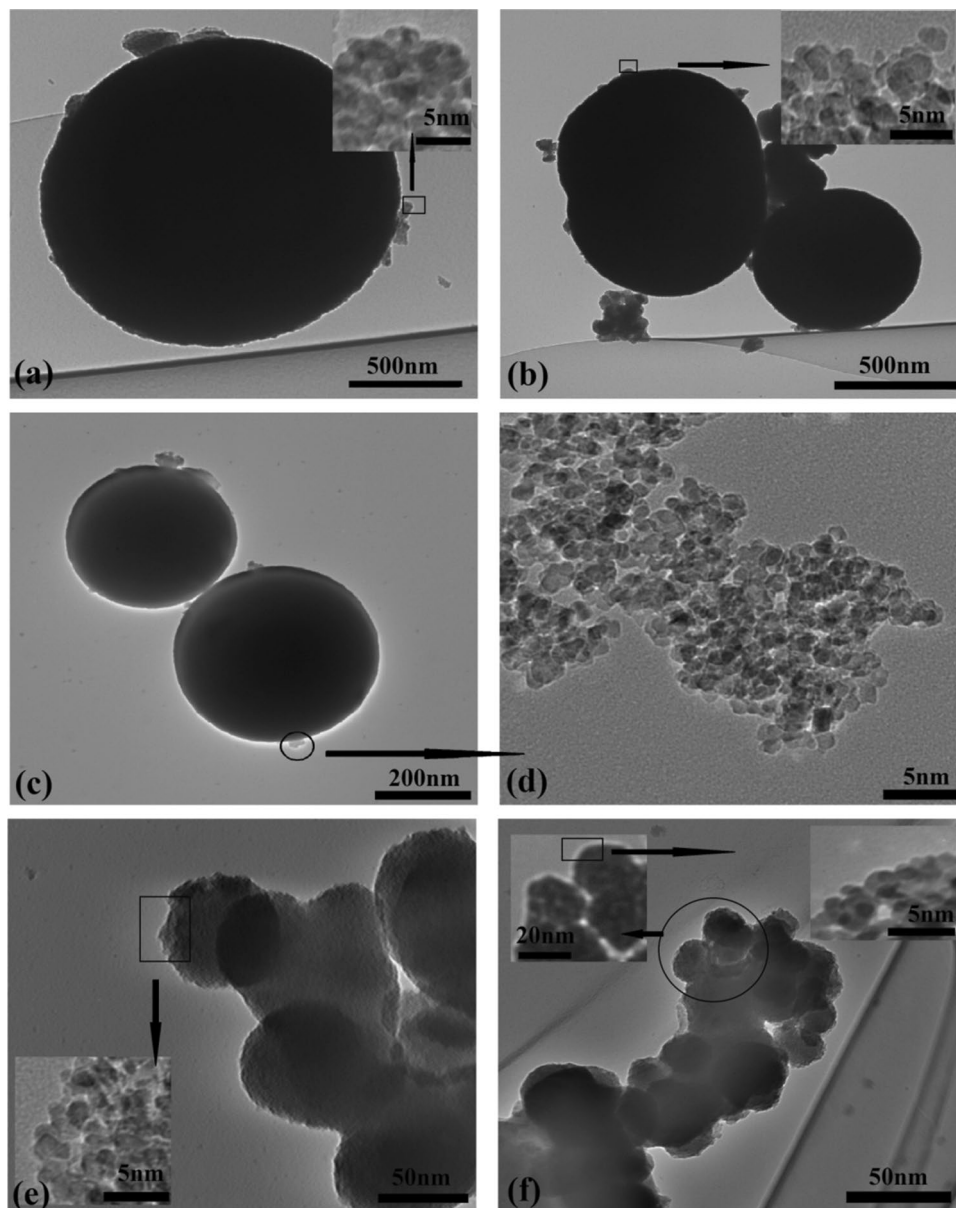
Figure 6. TEM images of (**a**) Tma, (**b**) Tmb, (**c**) Tmc, (**d**) magnified portion of Tmc, (**e**) Tmd, (**f**) Tme, and in the inset are the magnified portion of the corresponding images.

In Fig. 9c, the absorption spectra of CdS-TiO$_2$ are compared to those of bulk CdS and TiO$_2$ (anatase). Bulk CdS exhibited a sharp edge at 515 nm, while anatase TiO$_2$ exhibited one at 388 nm. The spectrum of CdS-TiO$_2$ NC displayed a mixture of these two spectra, with an absorption edge at 487 nm that was blue-shifted from that of pure CdS NP (515 nm) and at 388 nm corresponded to that of pure anatase TiO$_2$ NP. The synthesis of anatase TiO$_2$ in CdS-TiO$_2$ was shown to be good in accordance the XRD results. The creation of a solid solution at the interfaces as a result of close contact between CdS and TiO$_2$ caused this shift, and this behaviour determined the optical properties of the final nanostructure[91]. Which attributes to electronic semiconductor-support interaction (SEMSI) by several researchers[92,93]. The UV area is used to excite (bulk) TiO$_2$ (bandgap = 3.2 eV), whereas the visible region is used to excite CdS (bandgap 2.42 eV). As a result of visible light absorption, electrons in CdS nanoparticles can be stimulated from the valence band to the conduction band, forming electron–hole pairs that are then trapped by the surface state[94]. These electrons can transfer from the CdS to the TiO$_2$ conduction band. They can then migrate across the TiO$_2$ conduction band and contribute to the reduction of species like oxygen molecules or adsorbed pollutants[95]. In Fig. 9d, the bandgap curve of CdS-TiO$_2$ is compared to bulk CdS and TiO$_2$ (anatase) using the Tauc relation. Bulk CdS had a bandgap of 2.42 eV, while bulk TiO$_2$ had a bandgap of 3.2 eV. The bandgap curve of CdS-TiO$_2$ exhibited a combination of these two, with a bandgap of 3.2 eV for anatase TiO$_2$ NP and a bandgap of 2.55 eV for CdS NP.
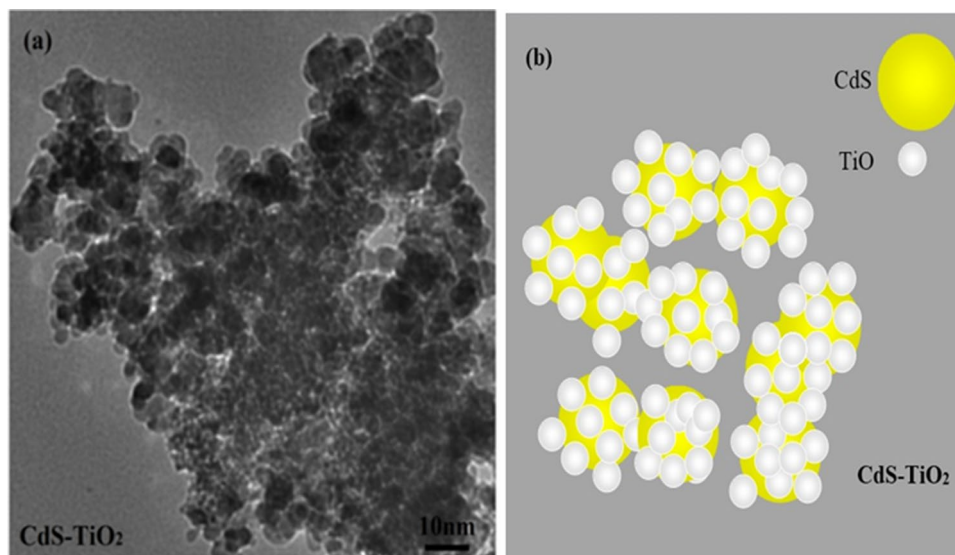
Figure 7. (**a**) The TEM image of the synthesized CdS-TiO$_2$ nanocomposite (**b**) A representative diagram of the synthesized CdS-TiO$_2$ nanocomposite.

Nanoparticles	Tma	Tmb	Tmc	Tmd	Tme	CdS-TiO$_2$
Particle size (nm)	1.5–2.0	1.5–1.7	1.2–1.5	1–1.2	0.8–1.0	5–6 (CdS), (TiO$_2$)

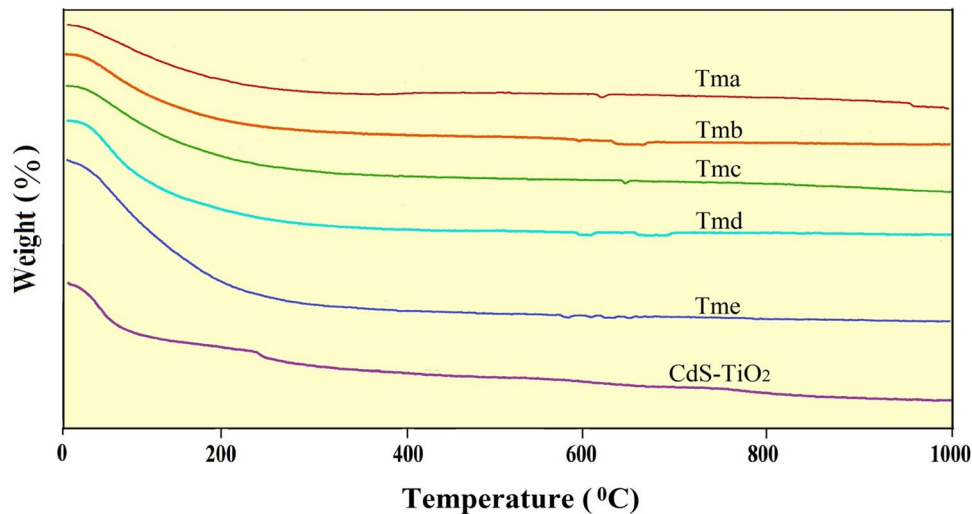**Table 2.** Average particle sizes of the synthesized TiO$_2$ NP (Tma, Tmb, Tmc, Tmd and Tme) and CdS-TiO$_2$ NC obtained by TEM.

Figure 8. TGA graphs of synthesized TiO$_2$ nanoparticles (Tma, Tmb, Tmc, Tmd and Tme) and CdS-TiO$_2$ nanocomposite.

Photocatalytic activity. The effect of samples synthesized in five distinct modes as catalysts on the removal of dye AB-29 was investigated, and the results are shown in Fig. 10a a relative change in AB-29 concentration (C/C$_0$) as a function of time in the presence and absence of photocatalysts. The activity of all five samples was compared in order to get superior photocatalytic activities of TiO$_2$ nanoparticles. UV light was used to conduct the photo-degradation investigations. Blank experiments were also separately carried out in presence of the photocatalyst under dark conditions and absence of the photocatalyst under irradiation. In both the cases, analysis of the samples did not show any appreciable loss of the dye (AB-29). The percentage of relative decolorization (C/C$_0$) of the dye AB-29 was determined in the following order: Tma (71%) Tmb (74%) Tmc (79%) Tmd (83%)

Nanoparticle	Absorption edge (nm)	Band gap (eV) (from Tauc curve)	Band gap (eV) ($E_g = 1240/\lambda_{onset}$)	Particle size (nm)
Tma	403	3.07	3.074	0.522
Tmb	393	3.14	3.155	0.208
Tmc	390	3.17	3.179	0.188
Tmd	388	3.2	3.195	0.161
Tme	382	3.25	3.246	0.125
CdS-TiO$_2$	487, 388	2.55, 3.2	2.546, 3.195	5.8, 0.161

Table 3. Absorption peaks and bandgap energy of the synthesized TiO$_2$ NP (Tma, Tmb, Tmc, Tmd and Tme) and CdS-TiO$_2$.
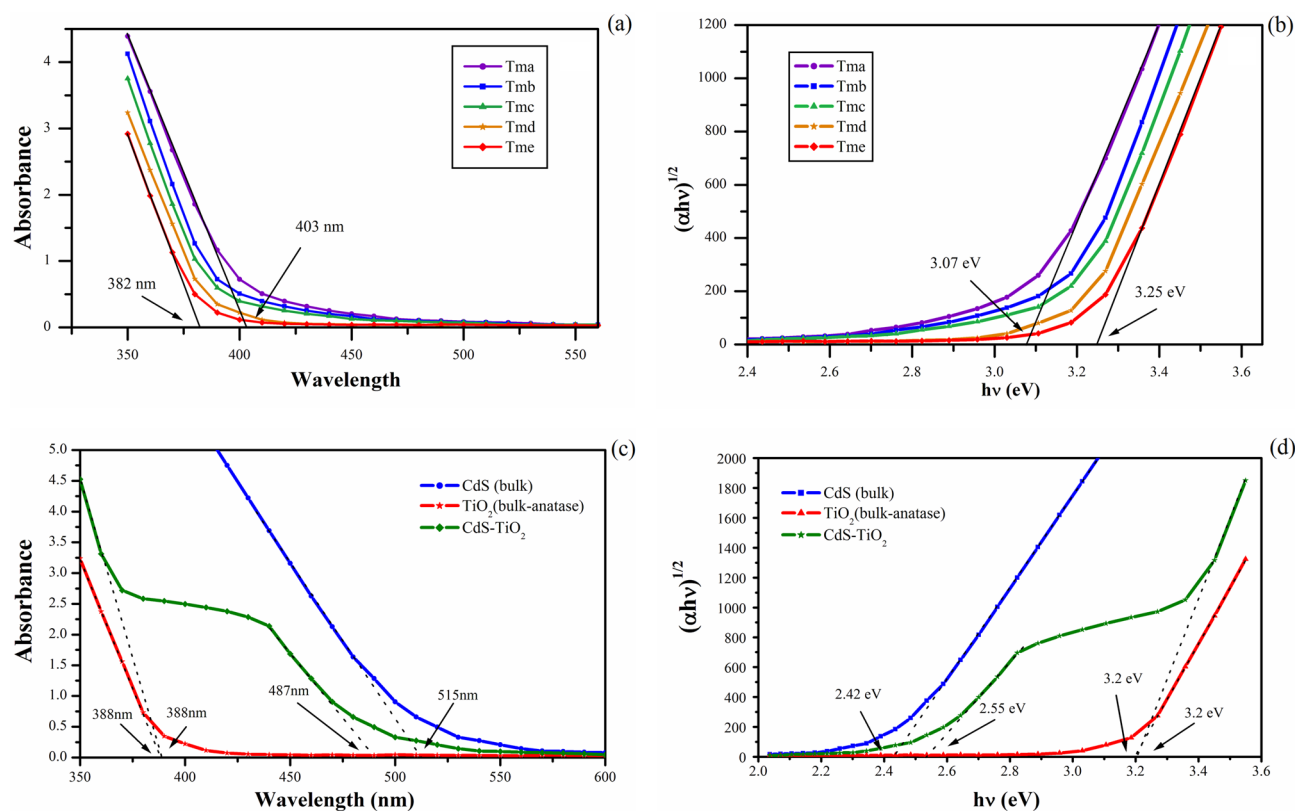
Figure 9. (**a**) The UV–Visible absorption spectrum of synthesized TiO$_2$ nanoparticles (Tma, Tmb, Tmc, Tmd and Tme) shows a slight blue shift in absorption edge. (**b**) The bandgap energy of the synthesized TiO$_2$ nanoparticles (Tma, Tmb, Tmc, Tmd and Tme). (**c**) The absorption spectra of CdS-TiO$_2$ with respect to pure CdS bulk and TiO$_2$ bulk. (**d**) Band gap energy curve of CdS-TiO$_2$ with respect to pure CdS and TiO$_2$ bulk.

Tme (86%). In the absence of photocatalyst, however, there was no discernible decrease in dye concentration. Multiple factors may have contributed to sample Tme's maximum photocatalytic activity.

Most dyes undergo photocatalytic decolorization according to the Langmuir–Hinshelwood kinetic model[96–98], which can be summarised as (2):

$$-dC/dt = kKC/(1 + KC) \tag{2}$$

where k represents the reaction rate constant (mMmin^{-1}), K represents the reactant's adsorption coefficient (mM^{-1}), and C represents the reactant concentration (mM). When C is very low, KC is minimal in comparison to unity, allowing Eq. (2) to be simplified to apparent pseudo-first-order kinetics[99].

$$-dC/dt = kKC = k_{app}C \tag{3}$$

The decolorization curve (Fig. 10a), emerged as an exponential decay curve which represents pseudo-first-order kinetics reasonably well. The rate constant was obtained for each experiment by plotting the natural logarithm of dye concentration as a function of irradiation time[100]. The following is a representation of the equation:
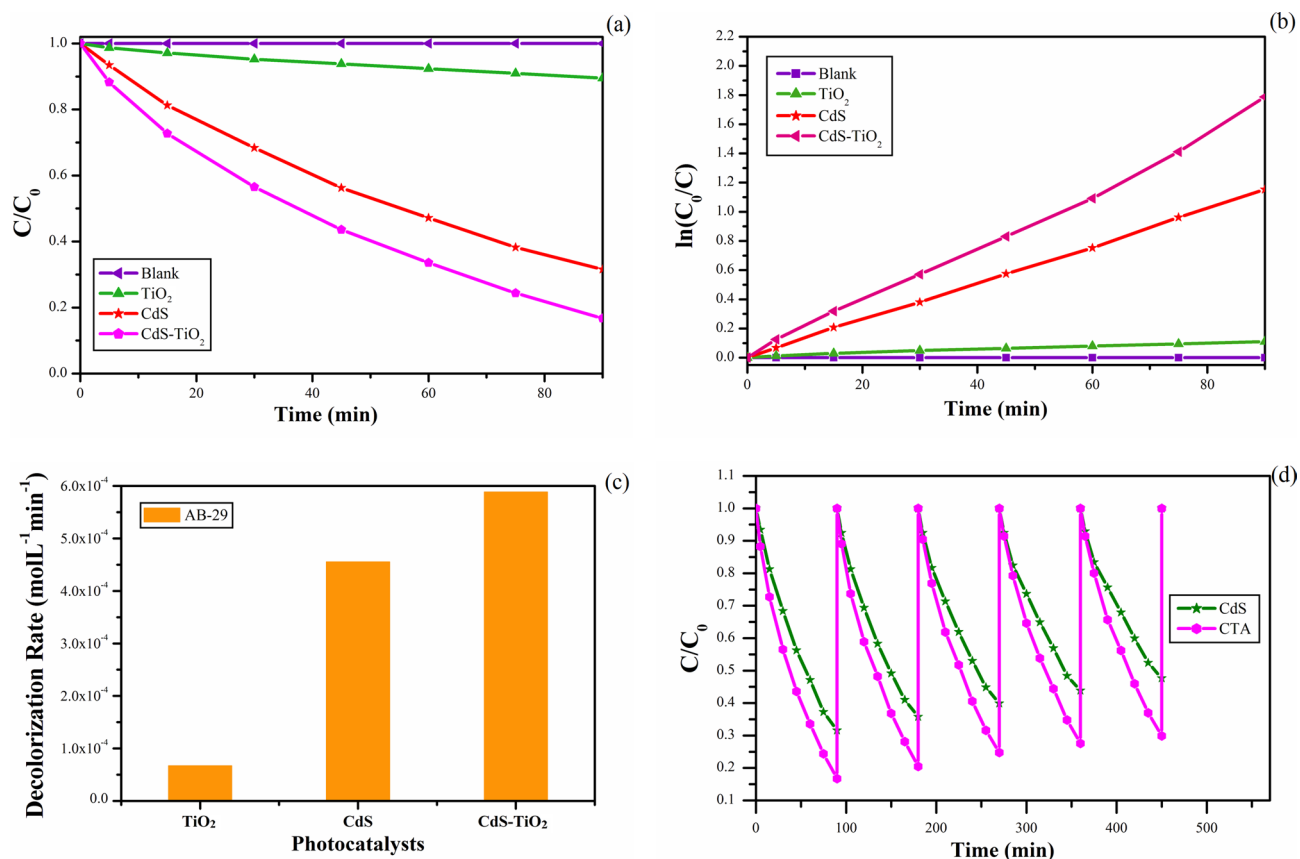
$$\ln (C_0/C) = k_{app}t \tag{4}$$

Figure 10. (**a**) Change in concentration of AB-29 with time in the presence and absence of synthesized TiO_2 nanoparticles (Tma, Tmb, Tmc, Tmd and Tme). (**b**) Change in concentration of AB-29 with time in the presence and absence of synthesized TiO_2 nanoparticles (Tma, Tmb, Tmc, Tmd and Tme). (**c**) The decolorization rate of AB-29 in the presence of different synthesized TiO_2 nanoparticles (Tma, Tmb, Tmc, Tmd and Tme). (**d**) Stability and recycle of TiO_2 nanocomposites (Tma, Tmb, Tmc, Tmd and Tme) for five consecutive cycles.

C_0 represents the starting reactant concentration (mM), C represents the reactant concentration (mM) at time "t", and k_{app} represents the apparent pseudo-first-order rate constant (min^{-1}).

The data in Fig. 10a were in good agreement with the pseudo-first-order reaction for our experimental conditions, as shown in Fig. 10b by plotting ln (C_0/C) versus irradiation time. For all of the experiments, the correlation constant (R^2) for the fitted lines was calculated to be 0.99.

The dye's degradation rate was estimated using the formula below[101]:

$$-(d[C])/dt \rightarrow k[C]^n \tag{5}$$

k = rate constant, C = concentration of the dye, n = order of reaction.

Tme exhibited the maximum activity and nearly fully decolorized the solution in only 90 min, according to the Kinetic findings. The decolorization rate of AB-29 in the presence of several photocatalysts (Tma, Tmb, Tmc, Tmd, and Tme) demonstrated that the decolorization of AB-29 continued faster as the diameters of the TiO_2 nanoparticles dropped (Fig. 10c). The decolorization rate followed the order; Tma (4.6×10^{-4}) < Tmb (4.8×10^{-4}) < Tmc (5.0×10^{-4}) < Tmd (5.3 xpas 10^{-4}) < Tme (5.5×10^{-4} mol L^{-1} min^{-1}). Increased catalyst surface area is responsible for the rise in photocatalytic efficiency when particle size decreases[102].

In addition, when particle size decreases, band gap energy rises, reducing charge carrier recombination. It is widely assumed that a bigger band gap equates to greater redox capacity[103]. As a result of its large surface area, enhanced bandgap, and strong redox capability with low photo corrosion, Tme had the highest photocatalytic activity. A photocatalytic reaction using TiO_2 is essentially a redox reaction including photogeneration, migration, trapping, and recombination of reactants adsorbed on its surface[104]. The process of photocatalysis over titanium dioxide (TiO_2) can be explained as follows: photocatalysis was initiated by the absorption of a photon with energy equal to or greater than the bandgap of TiO_2 (3.2 eV), leading to photo-excitation, producing electron–hole (e/h^+) pairs (Eq. 6)[105]. As a result, the TiO_2 particle operated as an electron donor or acceptor for molecules in the surrounding medium after irradiation. The photoexcited electron and hole took part in redox reactions with adsorbed species like water, hydroxide ions (OH), organic compounds, and oxygen. The photoexcitation of TiO_2 under UV light irradiation is depicted in Fig. 11 as an example scheme.

The holes (h^+) oxidized water (H_2O) Eq. (7) or hydroxyl anion (OH) Eq. (8) in the valence band to form the hydroxyl radical (·OH), a highly potent and indiscriminate oxidant. Similarly, the electron (e^-) reduced the
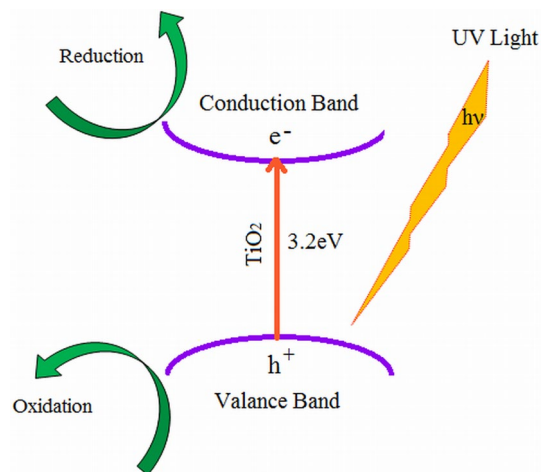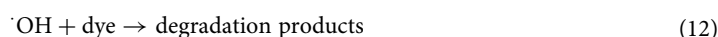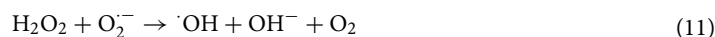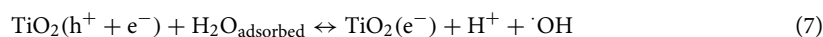
Figure 11. Schematic diagram of the photoexcitation of TiO_2 under UV light irradiation.

Cycle	Tma	Tmb	Tmc	Tmd	Tme
I	71.4	74.2	78.6	83.3	85.9
II	70.1	72.7	76.9	80.6	84.8
III	69.0	71.4	74.3	78.5	83.4
IV	67.8	70.4	72.7	76.8	82.1
V	66.7	68.9	71.4	74.4	80.5

Table 4. Decolorization rates of all the TiO_2 nanocatalysts (Tma, Tmb, Tmc, Tmd and Tme) for five consecutive cycles under UV light irradiation.

adsorbed O_2 to form superoxide radical anion ($O_2\cdot$) Eq. (9) and hydrogen peroxide (H_2O_2) Eq. (10), which interacted to produce the $\cdot OH$ radical Eq. (11). $\cdot OH$ radicals quickly attacked contaminants on the surface, as well as in solution Eq. (12). This prevented the electron from recombining with the hole and resulted in a concentration of oxygen radical species, which aided in the attack on pollutants[106,107].

The reactions can be expressed as follows:

$$TiO_2 + h\nu \leftrightarrow TiO_2(h^+ + e^-) \tag{6}$$

$$TiO_2(h^+ + e^-) + H_2O_{adsorbed} \leftrightarrow TiO_2(e^-) + H^+ + {}^{\cdot}OH \tag{7}$$

$$h^+ + OH^-_{adsorbed} \leftrightarrow {}^{\cdot}OH \tag{8}$$

$$e^- + O_2 \rightarrow O_2^{\cdot -} \tag{9}$$

$$2e^- + O_2 + 2H^+ \rightarrow H_2O_2 \tag{10}$$

$$H_2O_2 + O_2^{\cdot -} \rightarrow {}^{\cdot}OH + OH^- + O_2 \tag{11}$$

$${}^{\cdot}OH + dye \rightarrow degradation\ products \tag{12}$$

After 90 min of reaction time, the decolorization rates employing TiO_2 nanocatalysts (Tma, Tmb, Tmc, Tmd, and Tme) for the 5-cycling reuse are shown in Fig. 10d. Table 4 shows the results of five successive cycles of decolorization rates for all TiO_2 nanocatalysts (Tma, Tmb, Tmc, Tmd, and Tme). The catalytic activity of TiO_2 nanocatalysts (Tma, Tmb, Tmc, Tmd, and Tme) dropped marginally after the first cycles, according to the findings. Tme showed the most stability among them when compared to other TiO_2 nanocatalysts, which could be owing to Tme's small size.

Because the differences in relative stability among the TiO_2 NPs were not significant, it can be concluded that all of the produced TiO_2 NPs have good photocatalytic activity and UV light irradiation stability. However, because UV radiation accounts for just 4–6% of the total solar spectrum, it is vital to investigate TiO_2's applicability in the visible zone.
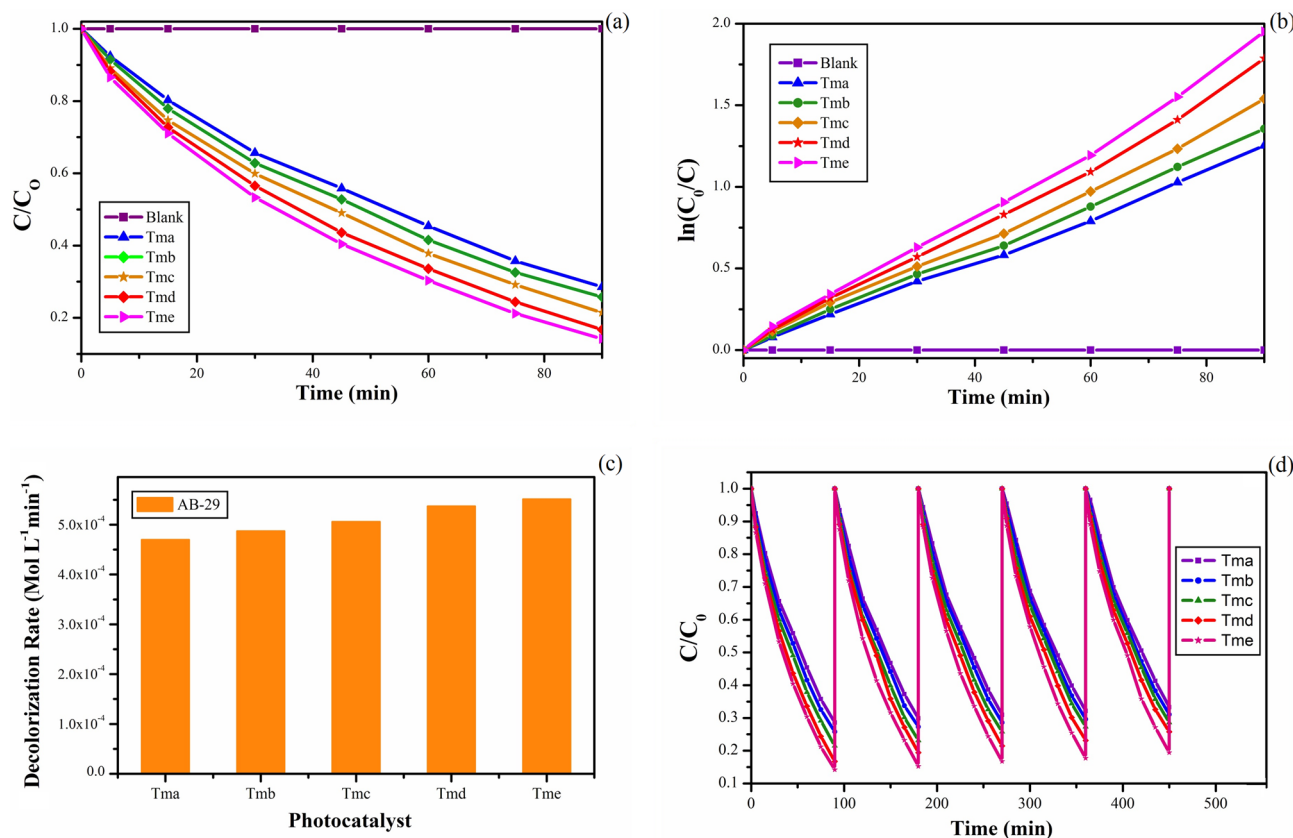
Figure 12. (**a**) Change in concentration of AB-29 with time in the presence and absence of synthesized CdS-TiO$_2$ nanoparticles in comparison to pure CdS and TiO$_2$ (**b**) Change in concentration of AB-29 with time in the presence and absence of synthesized CdS-TiO$_2$ nanoparticles in comparison to pure CdS and TiO$_2$. (**c**) The decolorization rate of AB-29 in the presence of different photocatalysts (TiO$_2$, CdS and CdS-TiO$_2$). (**d**) Stability and recycle of CdS-TiO$_2$ nanocomposite in comparison to pure CdS nanocomposite for five consecutive cycles.

As a result, TiO$_2$ NPs were combined with CdS NPs (CdS-TiO$_2$) and their photoactivity was investigated. A photo-degradation experiment using a dye derivative AB-29 in the presence of visible light was used to investigate the photocatalytic activity of CdS-TiO$_2$ nanoparticles. The photocatalytic experiment was conducted in the same manner as the TiO$_2$ NP experiment. The absorption edge of CdS-TiO$_2$ falls well inside visible radiation, resulting in enhanced photodegradation when exposed to visible light. In the presence of CdS-TiO$_2$ nanocomposite and ambient oxygen, irradiation of the dye under examination resulted in the decrease in absorption intensity as a function of irradiation time. In the presence and absence of CdS-TiO$_2$ photocatalysts, the relative change in the concentration of AB-29 (C/C$_0$) as a function of time is shown in Fig. 12a. The results were compared to nano-particles of TiO$_2$ (Degussa P-25) and CdS[55]. CdS-TiO$_2$ demonstrated 84% decolorization of AB-29 after 90 min of visible light irradiation, whereas CdS and TiO$_2$ showed only 68% and 09%, respectively, as shown in Fig. 12a. In the absence of photocatalyst, however, there was no discernible decrease in dye concentration. In the visible area, it was confirmed that CdS-TiO$_2$ NC had better photocatalytic activity than individual CdS and TiO$_2$ NP. The observations were consistent with a pseudo-first-order response, as illustrated in Fig. 12b by plotting ln (C$_0$/C) with irradiation time. A visualization of the natural logarithm of dye concentration as a function of irradiation duration Eq. (4) yielded the rate constant. The fitted lines' correlation constant (R^2) was calculated to be 0.99.

Using the Eq. (5), the dye degradation rate was estimated. The decolorization rate of AB-29 in the presence of CdS-TiO$_2$ photocatalyst as shown in Fig. 12c demonstrated that CdS-TiO$_2$ decolorized AB-29 was faster (5.8×10^{-4} mol L^{-1} min^{-1}) than CdS (4.5×10^{-4} mol L^{-1} min^{-1}) or TiO$_2$ (0.67×10^{-4} mol L^{-1} min^{-1}). The increased photocatalytic effectiveness of CdS-TiO$_2$ in the visible area was owing to reduced charge carrier recombination as a result of better charge separation and TiO$_2$ extension in response to visible light.

Figure 12d depicts the photodegradation of AB-29 by CdS-TiO$_2$ NC and CdS NP over a five-cycle period. After 90 min of response time, the relative decolorization utilising CdS-TiO$_2$ for the 5-cycling reuse was 83.3%, 79.6%, 75.4%, 72.4%, and 70.1%, respectively.

The catalytic activity of CdS-TiO$_2$ was declined after the first cycles but at a lower rate than that of pure CdS NP, which reduced at a faster rate (68.4%, 64.3%, 60.1%, 56.1% and 52.3% respectively for 5 consecutive cycles). As a result, CdS-TiO$_2$ appears to be a superior photocatalyst to pure CdS NP, with increased activity and stability. However, photo corrosion of CdS, which forms cadmium cations, may be the cause of the decrease in CdS-TiO$_2$ stability during photocatalytic degradation events.

Under the instance of CdS/TiO$_2$, the narrow band-gap allowed CdS/TiO$_2$ to absorb more photons, increasing TiO$_2$'s photocatalytic efficiency in the sun. The absorption of a photon by CdS with energy equal to or greater
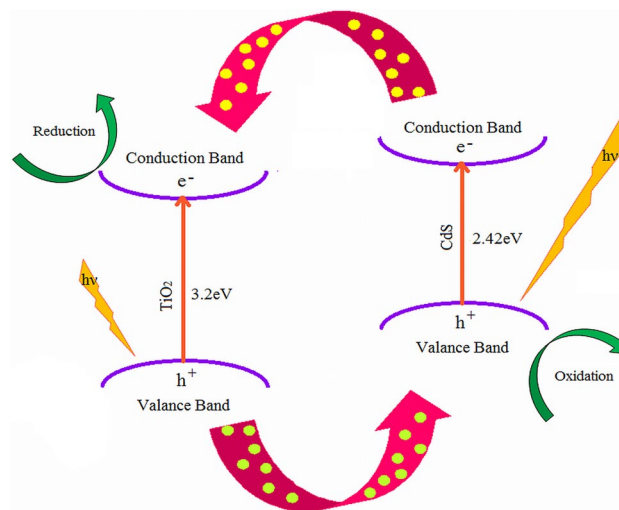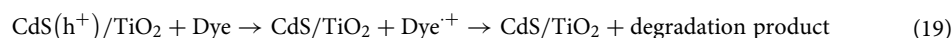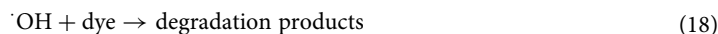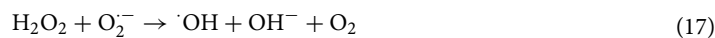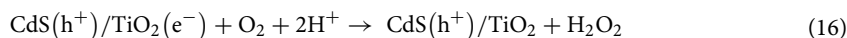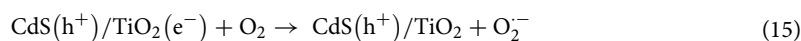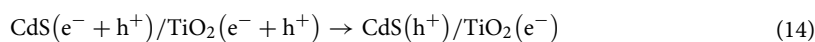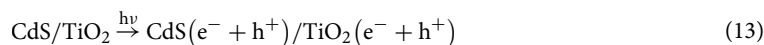
Figure 13. Schematic representation of photocatalytic mechanism followed by CdS-TiO$_2$.

than the bandgap of CdS (2.42 eV) (515 nm) caused excitation of electrons (e$^-$) from VB to CB of CdS, leaving a positive vacancy (hole, h$^+$) Eq. (13). TiO$_2$ also absorbed only a little quantity of visible light, causing photogenerated electrons and holes to occur in the CB and VB of TiO$_2$ Eq. (13). Because the conduction band (CB), valence band (VB), and band-gap of the two semiconductors were incompatible and overlapped, photogenerated electrons were directed from the CB of CdS to the CB of TiO$_2$, while photogenerated holes were directed from the VB of TiO$_2$ to the VB of CdS Eq. (14). Because holes flow in the opposite direction as electrons, they became trapped in the CdS. As a result, charge separation has improved, and recombination has decreased. A proposed mechanism for the degradation of contaminants on CdS coupled TiO$_2$ catalyst under visible light irradiation is given in Fig. 13 based on literature findings[13,19,79,89,91,92] and our experiment results.

In oxygen-equilibrated environments, the photoexcited and transmitted electrons in TiO$_2$'s CB were scavenged by molecular oxygen O$_2$, yielding the superoxide radical anion O$_2\cdot$ Eq. (15) and hydrogen peroxide H$_2$O$_2$ Eq. (16). The interaction of these intermediates resulted in the formation of the hydroxyl radical ·OH Eq. (17). The oxidative breakdown of AB-29 eq was then triggered by the ·OH radical Eq. (18)[91]. The photo-generated and transmitted hole in the VB of CdS cannot form hydroxyl radicals by oxidizing hydroxyl groups and H$_2$O molecules, but it can oxidize dye molecules to reactive intermediates and then to final products Eq. (19).

The reactions can be expressed as follows:

$$CdS/TiO_2 \xrightarrow{h\nu} CdS(e^- + h^+)/TiO_2(e^- + h^+) \tag{13}$$

$$CdS(e^- + h^+)/TiO_2(e^- + h^+) \rightarrow CdS(h^+)/TiO_2(e^-) \tag{14}$$

$$CdS(h^+)/TiO_2(e^-) + O_2 \rightarrow CdS(h^+)/TiO_2 + O_2^{\cdot-} \tag{15}$$

$$CdS(h^+)/TiO_2(e^-) + O_2 + 2H^+ \rightarrow CdS(h^+)/TiO_2 + H_2O_2 \tag{16}$$

$$H_2O_2 + O_2^{\cdot-} \rightarrow {}^{\cdot}OH + OH^- + O_2 \tag{17}$$

$${}^{\cdot}OH + dye \rightarrow degradation\ products \tag{18}$$

$$CdS(h^+)/TiO_2 + Dye \rightarrow CdS/TiO_2 + Dye^{\cdot+} \rightarrow CdS/TiO_2 + degradation\ product \tag{19}$$

Because photo-generated holes in CdS nanocrystals are unable to convert hydroxyl groups to hydroxyl radicals due to their valence band potential, photo corrosion of CdS occurs, resulting in the formation of cadmium cations[108–111]. The decrease in photo-stability of CdS-TiO$_2$ in the recycle experiment (Fig. 12d) also indicated leaching of cadmium cations. Table 5 provides additional examples of reports for the degradation performance of CdS and other nanocomposites for AB-29 azo dye as organic pollutants at the indicated experimental conditions.

Conclusion

Under ambient conditions, Titanium Dioxide nanoparticles (Tma, Tmb, Tmc, Tmd, and Tme) were effectively produced using a single pot chemical precipitation approach. The size of the TiO$_2$ nanocluster was reduced as the concentration of the Ti precursor dropped, as seen by the prepared TiO$_2$ NP. In all TiO$_2$ samples, a mixed crystalline phase was detected. The micrographic analysis demonstrated the production of spherical clusters

Catalyst	D (%)	Refs
Montmorillonite K10-Cu(II)ethylenediamine (MMTK10-Cu(en)2)	90	112
CdS	98	60
CdS with Sulphide ions	98	113
Fe (II) doped CdS	98.75	114
$ZnFe_2O_4$	98.83	115
CdS-TiO_2	84	Present work

Table 5. Comparative degradation of AB-29 azo dye by various nanocomposites.

whose diameters shrank drastically as the Ti precursor concentration dropped. With the decrease in Ti precursor concentration, the absorption spectra indicated a minor blue shift and, as a result, a slight rise in bandgap energies of TiO_2 NP was observed. Finally, under UV light, the photocatalytic response for the breakdown of the organic dye AB-29 was improved as TiO_2 had photoactive under UV light and CdS found as photocorroded during photocatalytic processes, an effort was made to combine the beneficial qualities of both CdS and TiO_2 while minimizing their disadvantages. A sandwich-type nanocomposite (CdS-TiO_2) of CdS with TiO_2 was also successfully synthesized. The CdS-TiO_2 showed good elemental purity and thermal stability. Cubic CdS and anatase TiO_2 were discovered in the XRD spectrum. Because of the presence of TiO_2, the absorption edge of CdS in CdS-TiO_2 shifted slightly blue, but the absorption edge of TiO_2 was identical to that of pure anatase TiO_2, indicating an improvement in the crystal structure. TiO_2's optical sensitivity was moved towards the visible range in CdS-TiO_2, allowing it to be photocatalytically active in visible light as well. With the decrease in Ti precursor concentration, the absorption spectra indicated a minor blue shift and, as a result, a slight rise in bandgap energies of TiO_2 NP.

References

1. Pawar, M., Topcu Sendoğdular, S. & Gouma, P. A brief overview of TiO_2 photocatalyst for organic dye remediation: Case study of reaction mechanisms involved in Ce-TiO_2 photocatalysts system. *J. Nanomater.* https://doi.org/10.1155/2018/5953609 (2018).
2. Perović, K. *et al.* Recent achievements in development of TiO_2-based composite photocatalytic materials for solar driven water purification and water splitting. *Materials* **13**(6), 1338. https://doi.org/10.3390/ma13061338 (2020).
3. Nagappan, S., Lee, D. B., Seo, D. J., Park, S. S. & Ha, C. Superhydrophobic mesoporous material as a pH-sensitive organic dye adsorbent. *J. Ind. Eng. Chem.* **22**, 288–295 (2015).
4. Thebo, K. H. *et al.* Highly stable graphene-oxide-based membranes with superior permeability. *Nat. Commun.* **9**, 1486 (2018).
5. Jung, K. *et al.* Aluminum carboxylate-based metal organic frameworks for effective adsorption of anionic azo dyes from aqueous media. *J. Ind. Eng. Chem.* **59**, 149–159 (2018).
6. Iqbal, M. *et al.* Photocatalytic degradation of organic pollutant with nanosized cadmium sulphide. *Mater. Sci. Energy Technol.* **2**(1), 41–45 (2018).
7. Fujishima, A. & Honda, K. Electrochemical photolysis of water at a semiconductor electrode. *Nature* **238**, 37–38 (1972).
8. Malato, S., Blanco, J., Vidal, A. & Richter, C. Photocatalysis with solar energy at a pilot-plant scale: An overview. *Appl. Catal. B* **37**, 1–15 (2002).
9. Preeti, S., Abdullah, M. M. & Ikram, S. Role of nanomaterials and their applications as photo-catalyst and sensors: A review. *Nano Res Appl.* **2**, 1 (2016).
10. Ejhieh, N. & Hushmandrad, S. Solar photodecolorization of methylene blue by CuO/X zeolite as a heterogeneous catalyst. *Appl. Catal. A* **388**, 149–159 (2010).
11. Lee, J. & Gouma, P. *Sol-Gel Processed Oxide Photocatalysts* (Springer, 2012).
12. Fulekar, M. H., Pathak, B. & Kale, R. K. In *Environment and Sustainable Development* (eds Envi Fulekar, M. *et al.*) (Springer, 2014).
13. Zyoud, A. H. *et al.* CdS-sensitized TiO_2 in phenazopyridine photo-degradation: catalyst efficiency, stability and feasibility assessment. *J. Hazard. Mater.* **173**, 318–325 (2010).
14. Singh, P., Abdullah, M., Sagadevan, S., Kaur, C. & Ikram, S. Highly sensitive ethanol sensor based on TiO2 nanoparticles and its photocatalyst activity. *Optik* **182**, 512–518 (2019).
15. Ohno, K., Tanaka, M., Takeda, J. & Kawazoe, Y. *Advances in Materials Research, Nano- and Micromaterials* Vol. 9 (Springer, 2008).
16. Kabra, K., Chaudhary, R. & Sawhney, R. L. Treatment of hazardous organic and inorganic compounds through aqueous-phase photocatalysis: A review. *Ind. Eng. Chem. Res.* **43**, 7683–7696 (2004).
17. Kim, E.-Y., Kim, D. S. & Ahn, B.-T. Synthesis of mesoporous TiO2 and its application to photocatalytic activation of methylene blue and *E. coli. Bull. Korean Chem. Soc.* **30**, 193–196 (2009).
18. Richards, R. *Surface and Nanomolecular Catalysis* (CRC/Taylor & Francis, 2006).
19. Shi, J.-W. *et al.* Low-temperature synthesis of CdS/TiO_2 composite photocatalysts: influence of synthetic procedure on photocatalytic activity under visible light. *J. Mol. Catal. A* **356**, 53–60 (2012).
20. Durgadevi, G., Samikannu, A., Chandran, M., Kuppusamy, M. R. & Dinakaran, K. Synthesis and characterization of CdS nanoparticle anchored Silica-Titania mixed Oxide mesoporous particles: Efficient photocatalyst for discoloration of textile effluent. *Int. J. Nano Dimens.* **10**(3), 272–280 (2019).
21. Moma, J. & Baloyi, J. Modified titanium dioxide for photocatalytic applications. *Photocatalysts* **3**, 38–56. https://doi.org/10.5772/intechopen.79374] (2019).
22. Li, D. *et al.* Effects of particle size on the structure and photocatalytic performance by alkali-treated TiO_2. *Nanomaterials* **10**, 546. https://doi.org/10.3390/nano10030546 (2020).
23. Michael, A. H. A surface science perspective on TiO2 photocatalysis. *Surf. Sci. Rep.* **66**, 185–297 (2011).

24. Brennan, P. J. *Laboratory and Accelerated Weathering Spectra Compared to Sunlight Through Automotive Glass* (The Q-Panel Company, 2011).
25. Sun, C. *et al.* Efficient fabrication of ZrO2-doped TiO2 hollow nanospheres with enhanced photocatalytic activity of rhodamine B degradation. *J. Colloid Interface Sci.* **364**, 288–297 (2011).
26. Sakthivel, S. *et al.* Enhancement of photocatalytic activity by metal deposition: Characterisation and photonic efficiency of Pt, Au and Pd deposited on TiO2 catalyst. *Water Res.* **38**, 3001–3008 (2004).
27. Nur, H., Misnon, I. I. & Wei, L. K. Stannic oxide-titanium dioxide coupled semiconductor photocatalyst loaded with polyaniline for enhanced photocatalytic oxidation of 1-octene. *Int. J. Photoenergy* **2007**, 1–6 (2007).
28. Bai, S., Li, H., Guan, Y. & Jiang, S. The enhanced photocatalytic activity of CdS/TiO2 nanocomposites by controlling CdS Dispersion on TiO2 nanotubes. *Appl. Surf. Sci.* **257**, 6406–6409 (2011).
29. Liu, G., Wang, L., Yang, H. G., Cheng, H.-M. & Lu, G. Q. M. Titania-based photocatalysts-crystal growth, doping and hetero-structuring. *J. Mater. Chem.* **20**, 831–843 (2010).
30. Monteiro, R. A., Lopes, F. V., Boaventura, R. A., Silva, A. M. & Vilar, V. J. Synthesis and characterization of N-modified titania nanotubes for photocatalytic applications. *Environ. Sci. Pollut. Res.* **22**, 810–819 (2015).
31. Szczepanik, B. Photocatalytic degradation of organic contaminants over clay-TiO2 nanocomposites: A review. *Appl. Clay Sci.* **141**, 227–239 (2017).
32. Etacheri, V., Di Valentin, C., Schneider, J., Bahnemann, D. & Pillai, S. C. Visible-light activation of TiO2 photocatalysts: Advances in theory and experiments. *J. Photochem. Photobiol. C* **25**, 1–29 (2015).
33. Moma, J. & Baloyi, J. Modified titanium dioxide for photocatalytic applications. In *Photocatalysts: Applications and Attributes* 37–56 (Intech, 2018).
34. Bhattacharyya, A., Kawi, S. & Ray, M. B. Photocatalytic degradation of orange II by TiO2 catalysts supported on adsorbents. *Catal. Today* **98**(3), 431–439 (2004).
35. Tang, Y. *et al.* Magnetic TiO2 -graphene composite as a high-performance and recyclable platform for efficient photocatalytic removal of herbicides from water. *J. Hazard. Mater.* **252**(253), 115–122 (2013).
36. Ivanova, I., Mendive, C. B. & Bahnemann, D. The role of nanoparticulate agglomerates in TiO2 photocatalysis: Degradation of oxalic acid. *J. Nanopart. Res.* **18**(7), 187 (2016).
37. Pellegrino, F. *et al.* Influence of agglomeration and aggregation on the photocatalytic activity of TiO2 nanoparticles. *Appl. Catal. B* **216**, 80–87 (2017).
38. Melcher, J., Barth, N., Schilde, C., Kwade, A. & Bahnemann, D. Influence of TiO2 agglomerate and aggregate sizes on photo-catalytic activity. *J. Mater. Sci.* **52**(2), 1047–1056 (2017).
39. Singh, N., Mondal, K., Misra, M., Sharma, A. & Gupta, R. K. Quantum dot sensitized electrospun mesoporous titanium dioxide hollow nanofibers for photocatalytic applications. *RSC Adv.* **6**(53), 48109–48119 (2016).
40. Misra, M., Singh, N. & Gupta, R. K. Enhanced visible-light-driven photocatalytic activity of Au@Ag core–shell bimetallic nanoparticles immobilized on electrospun TiO2 nanofibers for degradation of organic compounds. *Catal. Sci. Technol.* **7**(3), 570–580 (2017).
41. Singh, N., Prakash, J., Misra, M., Sharma, A. & Gupta, R. K. Dual functional Ta-doped electrospun TiO2 nanofibers with enhanced photocatalysis and SERS detection for organic compounds. *ACS Appl. Mater. Interfaces* **9**(34), 28495–28507 (2017).
42. Singh, N., Prakash, J. & Gupta, R. K. Design and engineering of high-performance photocatalytic systems based on metal oxide–graphene–noble metal nanocomposites. *Molecular Systems Design & Engineering* **2**, 422–439 (2017).
43. Tyagi, A., Tripathi, K. M., Singh, N., Choudhary, S. & Gupta, R. K. Green synthesis of carbon quantum dots from lemon peel waste: Applications in sensing and photocatalysis. *RSC Adv.* **6**(76), 72423–72432 (2016).
44. Dong, H. *et al.* An overview on limitations of TiO$_2$-based particles for photocatalytic degradation of organic pollutants and the corresponding countermeasures. *Water Res.* **79**, 128–146 (2015).
45. Low, J., Cheng, B. & Yu, J. Surface modification and enhanced photocatalytic CO2 reduction performance of TiO2: A review. *Appl. Surf. Sci.* **392**, 658–686 (2017).
46. Liu, N., Chen, X., Zhang, J. & Schwank, J. W. A review on TiO2 -based nanotubes synthesized via hydrothermal method: Formation mechanism, structure modification, and photocatalytic applications. *Catal. Today* **225**, 34–51 (2014).
47. Daghrir, R., Drogui, P. & Robert, D. Modified TiO$_2$ for environmental photocatalytic applications: A review. *Ind. Eng. Chem. Res.* **52**(10), 3581–3599 (2013).
48. Zhang, J., Xu, Q., Feng, Z. C., Li, M. J. & Li, C. Importance of the relationship between surface phases and photocatalytic activity of TiO$_2$. *Angew. Chem. Int. Ed.* **47**, 1766–1769 (2008).
49. Behnajady, M. A. & Eskandarloo, H. Silver and copper co-impregnated onto TiO$_2$-P25 nanoparticles and its photocatalytic activity. *Chem. Eng. J.* **228**, 1207–1213 (2013).
50. Chen, Y. S., Crittenden, J. C., Hackney, S., Sutter, L. & Hand, D. W. Preparation of a novel TiO$_2$-Based p−n junction nanotube photocatalyst. *Environ. Sci. Technol.* **39**, 1201–1208 (2005).
51. Arabatzis, I. M. *et al.* Silver-modified titanium dioxide thin films for efficient photodegradation of methyl orange. *Appl. Catal. B* **42**, 187–201 (2003).
52. Wang, C. Y., Bottcher, C., Bahnemann, D. W. & Dohrmann, J. K. A comparative study of nanometer sized Fe(III)-doped TiO$_2$ photocatalysts: Synthesis, characterization and activity. *J. Mater. Chem.* **13**, 2322–2329 (2003).
53. Burda, C. *et al.* Enhanced nitrogen doping in TiO$_2$ nanoparticles. *Nano Lett.* **3**, 1049–1051 (2003).
54. Cong, Y., Zhang, J. L., Chen, F., Anpo, M. & He, D. Preparation, photocatalytic activity, and mechanism of nano-TiO2 co-doped with nitrogen and iron (III). *J. Phys. Chem. C* **111**, 10618–10623 (2007).
55. Luo, H. *et al.* Photocatalytic activity enhancing for titanium dioxide by co-doping with bromine and chlorine. *Chem. Mater.* **16**, 846–849 (2004).
56. Wu, Y. M., Xing, M. Y., Zhang, J. L. & Chen, F. Effective visible light-active boron and carbon modified TiO$_2$ photocatalyst for degradation of organic pollutant. *Appl. Catal. B* **97**, 182–189 (2010).
57. Lu, N. *et al.* Fabrication of boron-doped TiO$_2$ nanotube array electrode and investigation of its photoelectrochemical capability. *J. Phys. Chem. C* **111**, 11836–11842 (2007).
58. Xie, W., Li, R. & Xu, Q. Enhanced photocatalytic activity of Se-doped TiO$_2$ under visible light irradiation. *Sci. Rep.* **8**, 8752. https://doi.org/10.1038/s41598-018-27135-4] (2018).
59. Qutub, N. *et al.* Synthesis, characterization and visible-light driven photocatalysis by differently structured CdS/ZnS sandwich and core–shell nanocomposites. *Physica E* **74**, 74–86 (2015).
60. Qutub, N., Pirzada, B. M., Umar, K. & Sabir, S. Synthesis of CdS nanoparticles using different sulfide ion precursors: Formation mechanism and photocatalytic degradation of Acid Blue-29. *J. Environ. Chem. Eng.* **4**, 808–817 (2016).
61. Qutub, N. & Sabir, S. Optical, thermal and structural properties of CdS quantum dots synthesized by a simple chemical route. *Int. J. Nanosci. Nanotechnol.* **8**(2), 111–120 (2012).
62. Qutub, N. & Sabir, S. Characterization of cadmium sulphide nanoparticles synthesized by chemical precipitation method. *Adv. Sci. Eng. Med.* **5**, 1–6 (2013).
63. Zhang, Y. J., Yan, W., Wu, Y. P. & Wang, Z. H. Synthesis of TiO2 nanotubes coupled with CdS nanoparticles and production of hydrogen by photocatalytic water decomposition. *Mater. Lett.* **62**, 3846–3848 (2008).

64. Pan, Y. X. *et al.* CdS quantum dots and tungsten carbide supported on anatase-rutile composite TiO_2 for highly efficient visible-light-driven photocatalytic H_2 evolution from water. *Catal. Sci. Technol.* **6**, 2206–2213 (2016).
65. Zhu, R., Yang, R., Hu, L. & Chen, B. Preparation of Z-Scheme system of CdS-RGO-BiVO$_4$ and its activity for hydrogen production. *Int. J. Hydrog. Energy* **44**, 25119–25128 (2019).
66. Chung, J., Kim, S. R. & Kim, J. O. Fabrication and characterization of CdS doped TiO2 nanotube composite and its photocatalytic activity for the degradation of methyl orange. *Water Sci Technol.* **72**(8), 1341–1347. https://doi.org/10.2166/wst.2015.318 (2015) (**PMID: 26465304**).
67. Rao, V. N. *et al.* Synthesis of titania wrapped cadmium sulfide nanorods for photocatalytic hydrogen generation. *Mater. Res. Bull.* **103**, 122–132 (2018).
68. Du, J. *et al.* Pyramid-like CdS nanoparticles grown on porous TiO_2 monolith: An advanced photocatalyst for H_2 production. *Electrochim. Acta* **250**, 99–107 (2017).
69. Buraso, W., Lachom, V., Siriya, P. & Laokul, P. Synthesis of TiO_2 nanoparticles via a simple precipitation method and photocatalytic performance. *Mater. Res. Express* **5**, 115003 (2018).
70. Beranek, R. & Kisch, H. Tuning the optical and photoelectrochemical properties of surface-modified TiO2. *Photochem. Photobiol. Sci.* **7**, 40–48 (2008).
71. Vasconcelos, D. C. L. *et al.* Infrared Spectroscopy of titania sol-gel coatings on 316L stainless steel. *Mater. Sci. Appl.* **2**, 1375–1382 (2011).
72. Crisan, M., Jitianu, A., Zaharescu, M., Mizukami, F. & Niwa, S. I. Sol-gel mono-and poly-component nanosized powders in the Al2O3–TiO2–SiO2–MgO system. *J. Dispers. Sci. Technol.* **24**, 129–144 (2003).
73. Socrates, G. *Infrared Characteristic Group Frequencies* (Wiley, 1980).
74. Nakamoto, K. *Infrared and Raman Spectra of Inorganic and Coordination Compounds* (Wiley Online Library, 1978).
75. El-Bially, A. B. *et al.* Preparation, Characterization And Physical Properties Of CdS nanoparticles with different sizes. *J. Appl. Sci. Res.* **8**, 676–685 (2012).
76. Lavand, A. B., Malghe, Y. S. & Singh, S. H. Synthesis, characterization, and investigation of visible light photocatalytic activity of C doped TiO_2/CdS core-shell nanocomposite. *Indian J. Mater. Sci.* https://doi.org/10.1155/2015/690568 (2015).
77. Singh, A., Goyal, V., Singh, J. & Rawat, M. Structural, morphological, optical and photocatalytic properties of green synthesized TiO2 NPs. *Curr. Res. Green Sustain. Chem.* **3**, 1000336. https://doi.org/10.1016/j.crgsc.2020.100033 (2020).
78. León, A. *et al.* FTIR and Raman characterization of TiO2 nanoparticles coated with polyethylene glycol as carrier for 2-methoxyestradiol. *Appl. Sci.* **7**, 49. https://doi.org/10.3390/app7010049 (2017).
79. Khiew, P. S., Huang, N. M., Radiman, S. & Ahmad, M. S. Synthesis and characterization of conducting polyaniline-coated cadmium sulphide nanocomposites in reverse microemulsion. *Mater. Lett.* **58**, 516–521 (2004).
80. Zhao, W., Bai, Z., Ren, A., Guo, B. & Wu, C. Sunlight photocatalytic activity of CdS modified TiO2 loaded on activated carbon fibers. *Appl. Surf. Sci.* **256**, 3493–3498 (2010).
81. Gu, L. *et al.* A novel incorporating style of polyaniline/TiO2 composites as effective visible photocatalysts. *J. Mol. Catal. A* **357**, 19–25 (2012).
82. Neppolian, B., Wang, Q., Jung, H. & Choi, H. Ultrasonic-assisted sol-gel method of preparation of TiO_2 nano-particles: characterization, properties and 4-chlorophenol removal application. *Ultrason. Sonochem.* **15**, 649–658 (2008).
83. Girginer, B., Galli, G., Chiellini, E. & Bicak, N. Preparation of stable CdS nanoparticles in aqueous medium and their hydrogen generation efficiencies in photolysis of water. *Int. J. Hydrog. Energy* **34**, 1176–1184 (2009).
84. Ma, L.-L. *et al.* Preparation, characterization and photocatalytic properties of CdS nanoparticles dotted on the surface of carbon nanotubes. *Nanotechnology* **19**, 115709 (2008).
85. Zubair, M., Svenum, I. H., Rønning, M. & Yang, J. Core-shell nanostructures of graphene-wrapped CdS nanoparticles and TiO2 (CdS@G@TiO2): The role of graphene in enhanced photocatalytic H2 generation. *Catalysts* **10**, 358. https://doi.org/10.3390/catal10040358 (2020).
86. Reghunath, S., Pinheiro, D. & Sunaja Devi, K. R. A review of hierarchical nanostructures of TiO2: Advances and applications. *Appl. Surf. Sci. Adv.* **3**, 100063 (2021).
87. Zhao, Y. *et al.* Enhanced photocatalytic activity of hierarchically micro-/nano-porous TiO2 films. *Appl. Catal. B* **83**, 24–29 (2008).
88. Paola, A. D. *et al.* Photocatalytic activity of nanocrystalline TiO2 (brookite, rutile and brookite-based) powders prepared by thermohydrolysis of TiCl4 in aqueous chloride solutions. *Colloids Surf. A* **317**, 366–376 (2008).
89. Satoh, N., Nakashima, T., Kamikura, K. & Yamamoto, K. Quantum size effect in TiO_2 nanoparticles prepared by finely controlled metal assembly on dendrimer templates. *Nat. Nanotechnol.* **3**, 106–111 (2008).
90. Maurya, A. & Chauhan, P. Structural and optical characterization of CdS/TiO_2 nanocomposite. *Mater. Charact.* **62**, 382–390 (2011).
91. Wongkalasin, P., Chavadej, S. & Sreethawong, T. Photocatalytic degradation of mixed azo dyes in aqueous wastewater using mesoporous-assembled TiO_2 nanocrystal synthesized by a modified sol-gel process. *Colloids Surf. A* **384**, 519–528 (2011).
92. Wu, L., Yu, J. C. & Fu, X. Characterization and photocatalytic mechanism of nanosized CdS coupled TiO2 nanocrystals under visible light irradiation. *J. Mol. Catal. A* **244**, 25–32 (2006).
93. Jang, J. S., Li, W., Oh, S. H. & Lee, J. S. Fabrication of CdS/TiO2 nano-bulk composite photocatalysts for hydrogen production from aqueous H2S solution under visible light. *Chem. Phys. Lett.* **425**, 278–282 (2006).
94. Weiß, H., Fernandez, A. & Kisch, H. Electronic semiconductor-support interaction: A novel effect in semiconductor photocatalysis. *Angew. Chem. Int. Ed.* **40**, 3825–3827 (2001).
95. Ullah, H., Viglašová, E. & Galamboš, M. Visible light-driven photocatalytic rhodamine B degradation using CdS nanorods. *Processes* **9**(2), 263. https://doi.org/10.3390/pr9020263 (2021).
96. Humayun, M., Raziq, F., Khan, A. & Luo, W. Modification strategies of TiO2 for potential applications in photocatalysis: A critical review. *Green Chem. Lett. Rev.* **11**(2), 86–102. https://doi.org/10.1080/17518253.2018.1440324 (2018).
97. Wu, C.-H., Chang, H.-W. & Chern, J.-M. Basic dye decomposition kinetics in a photocatalytic slurry reactor. *J. Hazard. Mater.* **137**, 336–343 (2006).
98. Dong, X., Ding, W., Zhang, X. & Liang, X. Mechanism and kinetics model of degradation of synthetic dyes by UV–vis/H2O2/ferrioxalate complexes. *Dyes Pigm.* **74**, 470–476 (2007).
99. Zhu, H. *et al.* Photocatalytic decolorization and degradation of congo red on innovative crosslinked chitosan/Nano-CdS composite catalyst under visible light irradiation. *J. Hazard. Mater.* **169**, 933–940 (2009).
100. Li, Y., Li, X., Li, J. & Yin, J. Photocatalytic degradation of methyl orange by TiO_2 coated activated carbon and kinetic study. *Water Res.* **40**, 1119–1126 (2006).
101. Alkaykh, S., Mbarek, A. & Ali-Shattle, E. E. Photocatalytic degradation of methylene blue dye in aqueous solution by MnTiO3 nanoparticles under sunlight irradiation. *Heliyon* **6**, e03663 (2020).
102. Chiu, Y. H., Chang, T. F., Chen, C. Y., Sone, M. & Hsu, Y. J. Mechanistic insights into photodegradation of organic dyes using heterostructure photocatalysts. *Catalysts* **9**(430), 1–32 (2019).
103. Li, D. *et al.* Effects of particle size on the structure and photocatalytic performance by alkali-treated TiO_2. *Nanomaterials* **10**(546), 2–14. https://doi.org/10.3390/nano10030546 (2020).
104. Zuo, C., Dorris, S. E., Balachandran, U. & Liu, M. Effect of Zr-doping on the chemical stability and hydrogen permeation of the Ni-BaCe0.8Y0.2O3-α mixed protonic-electronic conductor. *Chem. Mater.* **18**, 4647–4650 (2006).

105. Reijnders, L. Hazard reduction for the application of titania nanoparticles in environmental technology. *J. Hazard. Mater.* **152**, 440–445 (2008).
106. Al-Rasheed, R. A. Water treatment by heterogeneous photocatalysis: An overview. In *4th SWCC Acquired Experience Symposium* (2005).
107. Linsebigler, A. L. & Lu, G. Jr. Photocatalysis on TiO2 surfaces: Principles, mechanisms, and selected results. *Chem. Rev.* **95**, 735–758 (1995).
108. Hanaor, D. A. H. & Sorrell, C. C. Review of the anatase to rutile phase transformation. *J. Mater. Sci.* **46**, 855–874 (2011).
109. Tojo, F. *et al.* Histidine decorated nanoparticles of CdS for highly efficient h2 production via water splitting. *Energies* **13**(14), 3738. https://doi.org/10.3390/en13143738 (2020).
110. Kaushik, J. *et al.* Bio-mass derived functionalized graphene aerogel: A sustainable approach for the removal of multiple organic dyes and their mixture. *New J. Chem.* **45**, 9073–9083 (2021).
111. Kaushik, J., Kumar, V., Tripathi, K. M. & Sonkar, S. K. Sunlight-promoted photodegradation of Congo red by cadmium-sulfide decorated graphene aerogel. *Chemosphere* **287**, 132225 (2022).
112. Salema, I. A., El-Ghamryab, H. A. & El-Ghobashya, M. A. Beni-Suef Catalytic decolorization of acid blue 29 dye by H_2O_2 and a heterogeneous catalyst. *Univ. J. Basic Appl. Sci.* **3**, 186–192 (2014).
113. Pawar, M. J., Ingle, A. D. & Tayawade, R. K. Effect of synthesis parameters on photoactivity of CdS nanoparticles. *Chem. Sci. Trans.* **8**(2), 219–227. https://doi.org/10.7598/cst2019.1549 (2019).
114. Pawar, M. J., Ingle, A. D., Nimbalkar, V. B. & Taywade, R. K. Synthesis and characterization of Fe (II) doped CdS nanoparticles and photodegradation of acid blue–29 (AB-29) dye. *J. Nanosci. Technol.* **6**, 879–881. https://doi.org/10.30799/jnst.296.2006010 (2020).
115. Gönen, F. & Tekinerdoğan, G. Synthesis of specific ZnF based nanoparticles (ZnFe2O4): Antimicrobial properties, surface characteristics, and adsorption activity for AB 29 Textile Dye. *J. Nanotechnol.* https://doi.org/10.1155/2020/3139701 (2020).

Author contributions

Competing interests

The authors declare no competing interests.

Additional information

Correspondence and requests for materials should be addressed to N.Q., P.S., S.S. or W.-C.O.

Reprints and permissions information is available at www.nature.com/reprints.

Publisher's note Springer Nature remains neutral with regard to jurisdictional claims in published maps and institutional affiliations.